AFRL-PR-WP-TR-2006-2153

PROPULSION AND PWR RAPID RESPONSE RESEARCH AND DEVELOPMENT (R&D) SUPPORT

Delivery Order 0030: Study of Hot Deformation of Nanocomposite Rare Earth Magnets

By:
Shiqiang Sam Liu

University of Dayton Research Institute
Metals and Ceramics Division
300 College Park
Dayton, OH 45469-0170

For:
Universal Technology Corporation
1270 N. Fairfield Road
Dayton, OH 45432-2600

MARCH 2006

Final Report for 29 September 2003 – 28 February 2006

Approved for public release; distribution is unlimited.

STINFO COPY

PROPULSION DIRECTORATE
AIR FORCE MATERIEL COMMAND
AIR FORCE RESEARCH LABORATORY
WRIGHT-PATTERSON AIR FORCE BASE, OH 45433-7251

NOTICE

Using Government drawings, specifications, or other data included in this document for any purpose other than Government procurement does not in any way obligate the U.S. Government. The fact that the Government formulated or supplied the drawings, specifications, or other data does not license the holder or any other person or corporation; or convey any rights or permission to manufacture, use, or sell any patented invention that may relate to them.

This report was cleared for public release by the Air Force Research Laboratory Wright Site (AFRL/WS) Public Affairs Office (PAO) and is releasable to the National Technical Information Service (NTIS). It will be available to the general public, including foreign nationals.

PAO Case Number: AFRL/WS 06-1091, 26 April 2006

THIS TECHNICAL REPORT IS APPROVED FOR PUBLICATION.

//Signature//	//Signature//
JOHN C. HORWATH	C. SCOTT RUBERTUS
Electrical Engineer	Chief
Power Generation Branch	Power Generation Branch

This report is published in the interest of scientific and technical information exchange and its publication does not constitute the Government's approval or disapproval of its ideas or findings.

REPORT DOCUMENTATION PAGE

Form Approved
OMB No. 0704-0188

The public reporting burden for this collection of information is estimated to average 1 hour per response, including the time for reviewing instructions, searching existing data sources, searching existing data sources, gathering and maintaining the data needed, and completing and reviewing the collection of information. Send comments regarding this burden estimate or any other aspect of this collection of information, including suggestions for reducing this burden, to Department of Defense, Washington Headquarters Services, Directorate for Information Operations and Reports (0704-0188), 1215 Jefferson Davis Highway, Suite 1204, Arlington, VA 22202-4302. Respondents should be aware that notwithstanding any other provision of law, no person shall be subject to any penalty for failing to comply with a collection of information if it does not display a currently valid OMB control number. **PLEASE DO NOT RETURN YOUR FORM TO THE ABOVE ADDRESS**.

1. REPORT DATE *(DD-MM-YY)*	2. REPORT TYPE	3. DATES COVERED *(From - To)*
March 2006	Final	09/29/2003 – 02/28/2006

4. TITLE AND SUBTITLE

PROPULSION AND PWR RAPID RESPONSE RESEARCH AND DEVELOPMENT (R&D) SUPPORT
Delivery Order 0030: Study of Hot Deformation of Nanocomposite Rare Earth Magnets

5a. CONTRACT NUMBER
F33615-02-D-2299-0030

5b. GRANT NUMBER

5c. PROGRAM ELEMENT NUMBER
62203F

6. AUTHOR(S)

Shiqiang Sam Liu (University of Dayton Research Institute)

5d. PROJECT NUMBER
3145

5e. TASK NUMBER
21

5f. WORK UNIT NUMBER
30

7. PERFORMING ORGANIZATION NAME(S) AND ADDRESS(ES)

By:	For:
University of Dayton Research Institute Metals and Ceramics Division 300 College Park Dayton, OH 45469-0170	Universal Technology Corporation 1270 N. Fairfield Road Dayton, OH 45432-2600

8. PERFORMING ORGANIZATION REPORT NUMBER
UDR-TR-2006-00050

9. SPONSORING/MONITORING AGENCY NAME(S) AND ADDRESS(ES)

Propulsion Directorate
Air Force Research Laboratory
Air Force Materiel Command
Wright-Patterson AFB, OH 45433-7251

10. SPONSORING/MONITORING AGENCY ACRONYM(S)
AFRL-PR-WP

11. SPONSORING/MONITORING AGENCY REPORT NUMBER(S)
AFRL-PR-WP-TR-2006-2153

12. DISTRIBUTION/AVAILABILITY STATEMENT
Approved for public release; distribution is unlimited.

13. SUPPLEMENTARY NOTES
Report contains color.

PAO Case Number: AFRL/WS 06-1091, Clearance date: 26 Apr 2006.

14. ABSTRACT

High performance bulk anisotropic nanograin composite Nd2Fe14B/Fe and Nd2Fe14B/Fe-Co magnets were successfully synthesized using hot compacting blended Nd-Fe-B and –Fe-Co powders or coated ND-Fe-B powders followed by a subsequent hot deformation. Using both techniques, (BH)max could reach 45-55 MGOe. In addition, bulk anisotropic hybrid nanograin Pr2Fe14B/PrCo5 magnets with improved thermal stability were synthesized, and nanograin Sm2(Co, Fe) 17Fe-Co magnets were studied.

15. SUBJECT TERMS

composite magnets high temperature, hot compaction, hot deformation, hybrid magnets, interface exchange coupling, nanocomposite, nanograin magnets, nanostructure, Nd2Fe14B, permanent magnets, powder coating. Sm2(Co, Fe)17, thermal stability

16. SECURITY CLASSIFICATION OF:			17. LIMITATION OF ABSTRACT:	18. NUMBER OF PAGES	19a. NAME OF RESPONSIBLE PERSON (Monitor)
a. REPORT	b. ABSTRACT	c. THIS PAGE			John Horwath
Unclassified	Unclassified	Unclassified	SAR	58	19b. TELEPHONE NUMBER *(Include Area Code)* N/A

Standard Form 298 (Rev. 8-98)
Prescribed by ANSI Std. Z39-18

TABLE OF CONTENTS

SECTION		PAGE
	Abstract	1
1	High-Performance Nanograin Composite $Nd_2Fe_{14}B/\alpha$-Fe and $Nd_2Fe_{14}B$/Fe-Co Magnets	2
	1.1 Magnets prepared by using powder blending technique	2
	1.1.1 Magnets prepared by blending a melt-spun Nd-rich Nd-Fe-B powder and a commercial α-Fe or Fe-Co powder	2
	1.1.2 Magnets prepared by using special powder blending techniques	9
	1.1.3 Magnets prepared by blending Nd-Fe-B powder with α-Fe nanoparticles	10
	1.1.4 Magnets prepared by blending Nd-Fe-B powder with Fe-Co-B ribbons	10
	1.2 Magnets prepared by using coating technologies	11
	1.2.1 Magnets prepared by using DC and RF sputtering techniques	11
	1.2.2 Magnets prepared by using PLD technique	14
	1.2.3 Magnets prepared by using chemical coating technique	14
	1.2.4 Magnets prepared using electrolyte coating technique	16
	1.2.5 Effect of original particle size	21
	1.2.6 Effect of hot deformation temperature	23
	1.3 Advantage of the nanograin composite magnets	23
	1.3.1 Problem with current nanograin composite magnets	25
2	Hybrid Nanograin $Pr_2(Fe,Co)_{14}B/Pr(Co,Fe)_5$ Magnets with Improved Thermal Stability	27
	2.1 Nanograin $PrCo_5$ and $Pr(Co,Fe)_5$ magnets	27
	2.2 Nanograin $Pr_2(Fe,Co)_{14}B$ magnets	28
	2.3 Nanocomposite $Pr_2(Fe,Co)_{14}B/PrCo_5$ and $Pr_2(Fe,Co)_{14}B/Pr(Co,Fe)_5$ magnets	29
	2.3.1 Magnetic properties of nanocomposite $Pr_2(Fe,Co)_{14}B/PrCo_5$ and $Pr_2(Fe,Co)_{14}B/ Pr(Co,Fe)_5$ magnets	29
	2.3.2 Thermal stability of nanocomposite $Pr_2(Fe,Co)_{14}B/ Pr(Co,Fe)_5$ magnets	31
	2.3.3 Microstructure of nanocomposite $Pr_2(Fe,Co)_{14}B/ Pr(Co,Fe)_5$ magnets	32
	2.3.4 Novel coercivity enhancement after hot deformation	33
	2.3.5 Long-term stability of the nanograin structure of hybrid nanocomposite magnets	38
3	Nanograin Composite $Sm_2(Co,Fe)_{17}$/Fe-Co Magnets	39
4.	Conclusions	42
5.	References	43

LIST OF ILLUSTRATIONS

FIGURE		PAGE
1.1	α-Fe powder particles used in this project.	3
1.2	Cross section of α-Fe powder particles.	3
1.3	Fe-Co powder particles used in this project.	3
1.4	SEM micrograph of a fracture surface of a Fe-Co particle.	4
1.5	SEM back-scattered electron image of a hot deformed composite $Nd_{13.5}Fe_{80}Ga_{0.5}B_6$/ α -Fe (91.7 wt%/8.3 wt%) magnet.	4
1.6	SEM back-scattered electron image of a hot deformed composite $Nd_{14}Fe_{79.5}Ga_{0.5}B_6$/Fe-Co (95 wt%/5 wt%) magnet.	5
1.7	Demagnetization curves of an anisotropic $Nd_{14}Fe_{79.5}Ga_{0.5}B_6$/α-Fe (95 wt%/5 wt%) magnet.	5
1.8	Demagnetization curves of an anisotropic $Nd_{14}Fe_{79.5}Ga_{0.5}B_6$/Fe-Co (97 wt%/3 wt%) magnet.	5
1.9	Effects of the α-Fe content on B_r and $_MH_c$ of nanograin composite $Nd_{14}Fe_{79.5}Ga_{0.5}B_6$/α-Fe magnets.	6
1.10	Effects of the α-Fe content on $(BH)_{max}$ of nanograin composite $Nd_{14}Fe_{79.5}Ga_{0.5}B_6$/α-Fe magnets.	6
1.11	Effects of the α-Fe content on B_r and $_MH_c$ of nanograin composite $Nd_{14}Fe_{79.5}Ga_{0.5}B_6$/α-Fe magnets.	7
1.12	Effects of Fe-Co fraction on $(BH)_{max}$ of composite $Nd_{14}Fe_{79.5}Ga_{0.5}B_6$/Fe-Co magnets.	7
1.13	Comparison of XRD patterns of (a) a composite $Nd_2Fe_{14}B$/α-Fe magnet with $(BH)_{max}$ ~40 MGOe prepared by blending a Nd-rich Nd-Fe-B powder with a Nd-poor Nd-Fe-B powder, (b) a composite Nd-Fe-B/α -Fe magnet with $(BH)_{max}$ ~50 MGOe prepared by blending a Nd-rich Nd-Fe-B powder with an α-Fe powder, and (c) a commercial sintered Nd-Fe-B magnet with $(BH)_{max}$ ~40 MGOe.	8
1.14	A TEM micrograph of a $Nd_{13.5}Fe_{80}Ga_{0.5}B_6$/α-Fe (95 wt%/5 wt%) magnet with $(BH)_{max}$ = 48 MGOe.	8
1.15	A TEM micrograph of a composite $Nd_{13.5}Fe_{80}Ga_{0.5}B_6$/α-Fe (95 wt%/5 wt%) magnet showing hard/soft interface.	9
1.16	SEM backscattered electron image of the $Nd_2Fe_{14}B$/α-Fe (96 wt%/4 wt%) magnet specimen.	10
1.17	A SEM micrograph of Nd-Fe-B powder particles after DC sputtering.	12
1.18	A SEM micrograph of a coated surface of a Nd-Fe-B powder particle after DC sputtering.	12
1.19	SEM/EDS of a coated surface of Nd-Fe-B powder particle.	12

FIGURE		PAGE
1.20	Demagnetization curves of a composite $Nd_{14}Fe_{79.5}Ga_{0.5}B_6$/Fe-Co magnet prepared using DC sputtering for 8 hours.	13
1.21	Demagnetization curves of a composite $Nd_{14}Fe_{79.5}Ga_{0.5}B_6$/Fe-Co magnet prepared using DC sputtering for 21 hours.	13
1.22	Demagnetization curves of a composite $Nd_{14}Fe_{79.5}Ga_{0.5}B_6$/Fe-Co magnet prepared using PLD for 6 hours.	14
1.23	Demagnetization curves of a composite $Nd_{14}Fe_{79.5}Ga_{0.5}B_6$/Fe-Co magnet prepared using chemical coating for 1 hour with $(BH)_{max}$ = 48.8 MGOe.	15
1.24	Demagnetization curves of a composite $Nd_{14}Fe_{79.5}Ga_{0.5}B_6$/Fe-Co magnet prepared using chemical coating for 1 hour with $(BH)_{max}$ = 49.06 MGOe.	15
1.25	Apparatus for electrolyte coating.	16
1.26	SEM micrographs of the surfaces of Nd-Fe-B particles coated using electrolyte coating with different magnifications.	17
1.27	SEM/EDS of the surface of a Nd-Fe-B particle coated using electrolyte coating.	17
1.28	Demagnetization curves of a composite $Nd_{14}Fe_{79.5}Ga_{0.5}B_6/\alpha$-Fe magnet prepared using electrolyte coating for 30 minutes.	18
1.29	SEM micrograph of a composite $Nd_{14}Fe_{79.5}Ga_{0.5}B_6/\alpha$-Fe magnet prepared using electrolyte coating.	18
1.30	SEM/EDS of a composite $Nd_{14}Fe_{79.5}Ga_{0.5}B_6$/Fe magnet prepared using electrolyte coating.	19
1.31	TEM micrograph of a $Nd_{14}Fe_{79.5}Ga_{0.5}B_6/\alpha$-Fe magnet prepared using electrolyte coating.	19
1.32	TEM micrograph of a $Nd_{14}Fe_{79.5}Ga_{0.5}B_6/\alpha$-Fe magnet prepared using electrolyte coating, showing Nd-Fe-B grains and a minor Nd-rich phase.	20
1.33	Demagnetization curves of hot deformed $Nd_2Fe_{14}B$/Fe-Co magnet prepared using electric coating with powder particle size of -80+140 mesh.	22
1.34	Demagnetization curves of hot deformed $Nd_2Fe_{14}B$/Fe-Co magnet prepared using chemical coating with powder particle size of -80+140 mesh.	22
1.35	Demagnetization curves of hot deformed $Nd_2Fe_{14}B$/Fe-Co magnet prepared using chemical coating with powder particle size of +80mesh.	23
1.36	Magnetic properties vs. hot deformation temperature.	24
1.37	Comparison of processes of (a) conventional sintered Nd-Fe-B magnets; (b) new nanograin composite Nd-Fe-B/α-Fe or Nd-Fe-B/Fe-Co magnets.	24
1.38	XRD pattern of the no-mark surface of specimen HD915.	25
1.39	XRD pattern of the mark surface of specimen HD915.	26
1.40	Demagnetization curves of specimen HD915.	26

LIST OF ILLUSTRATIONS (Continued)

FIGURE		PAGE
2.1	Demagnetization curves of hot compacted and hot deformed nanograin $PrCo_5$.	27
2.2	Effect of Fe content, x, in $Pr(Co_{1-x}Fe_x)_5$ on magnetic properties of $Pr(Co_{1-x}Fe_x)_5$.	28
2.3	Demagnetization curves of hot compacted isotropic $Pr_2(Fe_{0.94}Co_{0.06})_{14}B$ and hot deformed anisotropic $Pr_2(Fe_{0.94}Co_{0.06})_{14}B$.	28
2.4	Demagnetization curves of the first bulk hot deformed nanocrystalline $Pr_2(Fe_{0.94}Co_{0.06})_{14}B/PrCo_5$ [80 wt%/20 wt%] magnet.	29
2.5	Magnetic properties as a function of the fraction of $PrCo_5$ in a hybrid $Pr_2(Fe_{0.94}Co_{0.06})_{14}B/PrCo_5$ magnet.	29
2.6	Demagnetization curves of the first bulk hot deformed nanocomposite $Pr_2(Fe_{0.94}Co_{0.06})_{14}B/Pr(Co_{0.8}Fe_{0.2})_5$ [80 wt%/20 wt%].	30
2.7	Demagnetization curves of the first bulk hot deformed nanocomposite $Pr_2(Fe_{0.94}Co_{0.06})_{14}B/Pr(Co_{0.8}Fe_{0.3})_5$ [80 wt%/20 wt%].	30
2.8	Effect of Fe content, x, in $Pr_2(Fe,Co)_{14}B/Pr(Co_{1-x}Fe_x)_5$ on $(4\pi M)_{max}$, B_r, ${}_MH_c$, and H_k of hybrid nanocrystalline $Pr_2(Fe,Co)_{14}B/Pr(Co_{1-x}Fe_x)_5$.	31
2.9	Temperature coefficient of magnetic flux versus temperature for (a) $Pr_2(Fe_{0.94}Co_{0.06})_{14}B$; (b) hybrid $Pr_2(Fe_{0.94}Co_{0.06})_{14}B/Pr(Co_{0.8}Fe_{0.2})_5$ [80 wt%/20 wt%]; (c) hybrid $Pr_2(Fe_{0.94}Co_{0.06})_{14}B/Pr(Co_{0.8}Fe_{0.2})_5$ [60 wt%/40 wt%]; and (d) $Pr(Co_{0.8}Fe_{0.2})_5$.	31
2.10	SEM micrographs of anisotropic hybrid $Pr_2(Fe_{0.94}Co_{0.06})_{14}B/Pr(Co_{0.8}Fe_{0.2})_5$ [60 wt%/40 wt%]with small (a) and large magnifications (b).	32
2.11	Demagnetization curves of hot pressed and hot deformed $Pr_2(Fe_{0.94}Co_{0.06})_{14}B/Pr(Co_{0.5}Fe_{0.5})_5$ [80 wt%/20 wt%].	33
2.12	Demagnetization curves of hot pressed and hot deformed $Pr_2(Fe_{0.94}Co_{0.06})_{14}B/Pr(Co_{0.8}Fe_{0.2})_5$ [60 wt%/40 wt%].	34
2.13	Demagnetization curves of hot pressed and hot deformed $Pr_2(Fe_{0.94}Co_{0.06})_{14}B/Pr(Co_{0.7}Fe_{0.3})_5$ [60 wt%/40 wt%].	34
2.14	XRD pattern of a powder mixture of $Pr_2(Fe_{0.94}Co_{0.06})_{14}B/Pr(Co_{0.7}Fe_{0.3})_5$ [60 wt%/40 wt%] after mechanical alloying.	35
2.15	XRD pattern of hot compacted $Pr_2(Fe_{0.94}Co_{0.06})_{14}B/Pr(Co_{0.7}Fe_{0.3})_5$ [60 wt%/40 wt%].	35
2.16	XRD pattern of a hot deformed $Pr_2(Fe_{0.94}Co_{0.06})_{14}B/Pr(Co_{0.7}Fe_{0.3})_5$ [60 wt%/40 wt%] on the no mark surface, showing crystallized 2:14:1 and 1:5 phases with relatively poor grain alignment.	36
2.17	XRD pattern of the hot deformed $Pr_2(Fe_{0.94}Co_{0.06})_{14}B/Pr(Co_{0.7}Fe_{0.3})_5$ [60 wt%/40 wt%] on the marked surface, showing crystallized 2:14:1 and 1:5 phases with good grain alignment.	36

FIGURE		PAGE
2.18	Temperature dependence of magnetic moment of $Pr_2(Fe_{0.94}Co_{0.06})_{14}B$/ $Pr(Co_{0.7}Fe_{0.3})_5$ [60 wt%/40wt%], showing two major events at 505°C and 975°C and minor events.	37
2.19	SEM backscattered electron image of $Pr_2(Fe_{0.94}Co_{0.06})_{14}B/Pr(Co_{0.7}Fe_{0.3})_5$ [60 wt%/40wt%] after hot deformation, showing 2:14:1 matrix phase and 1:5 minor phase.	37
2.20	Three zones in the microstructure of $Pr_2(Fe_{0.94}Co_{0.06})_{14}B/Pr(Co_{0.7}Fe_{0.3})_5$ [60 wt%/40wt%].	38
2.21	Result of a long-term aging experiment of a nanocomposite $Nd_2(Fe_{0.94}Co_{0.06})_{14}B/Sm_2(Co_{0.7}Fe_{0.3})_{17}$ [80 wt%-20 wt%] magnet with L/D = 1 aged at 100°C in air.	39
3.1	Comparison of processes used to make nanograin composite $Sm_2(Co,Fe)_{17}$/ Fe-Co (a) and conventional sintered $Sm_2(Co,Fe,Cu,Zr)_{17}$ magnets (b).	40
3.2	Demagnetization curves of hot pressed $Sm(Co_{0.75}Fe_{0.11}Cu_{0.11}Zr_{0.03})_{7.3}$.	41
3.3	Demagnetization curves of hot deformed $Sm(Co_{0.75}Fe_{0.11}Cu_{0.11}Zr_{0.03})_{7.3}$.	41
3.4	Demagnetization curves of hot deformed $Sm(Co_{0.75}Fe_{0.11}Cu_{0.11}Zr_{0.03})_{7.3}$ after subsequent heat treatment.	42

LIST OF TABLES

TABLE		PAGE
1-1	Comparison of Grain Alignment Represented by $H_k/_MH_c$ and $4\pi M$ at $(BH)_{max}/(4\pi M)_{max}$	20
1-2	Effect of Original Nd-Fe-B Particle Size on Magnetic Properties of Composite Nd-Fe-B/Fe-Co Magnets Preparing Using Different Coating Techniques	21
2-1	Compositions of Three Zones Obtained from SEM/EDS Analyses	38

FOREWORD

The work documented in this report was performed by the University of Dayton between October 2004 and February 2006, for Universal Technology Corporation, Dayton, Ohio. The effort was performed as Delivery Order 30 on Contract No. F33615-02-D-2299, Subcontract No. 05-S530-0030-01.

Technical support and direction of this Delivery Order was provided by Dr. John Horwath. Dr. Shiqiang (Sam) Liu was the Delivery Order Principal Investigator. Mr. Don Lee also supported the execution of this Delivery Order.

The author wishes to acknowledge the assistance of Mr. Scott Bauser, Ms. Ashil Higgins, Mr. Jacob Lawson, and Mr. Adam Wangler for their technical support, Ms. Niki Maxwell for technical report editing, and Ms. Sheila Liskany of the University of Dayton Research Institute, who provided the administrative support to make this work possible.

Final Technical Report

Prime Grant Number: F33615-02-D-2299; Subcontract No. 05-S530-0030-01-C2

Program: AFRL/PRPG, DO 0030

Contract Title: High-Performance Nanostructured Rare Earth Magnets

Reporting Period: 12 Dec 04 through 11 Jan 05

Contract Objective / Approach:

The objectives of this research project were to develop innovative technologies and cost-effective manufacturing processes for synthesizing high-performance bulk nanostructured magnets for applications in Air Force systems with significantly enhanced system performance and reliable operation. The program objectives also included developing novel nanostructured rare earth magnets with high operating temperature and improved thermal stability of magnetic performance.

The technical approach included the following tasks:

- Study and optimize the rapid inductive compaction and hot deformation processes.
- Study the effect of compositions and a small amount of additives.
- Study Nd-Fe-B and α-Fe powder blending process.
- Apply techniques developed in $Nd_2Fe_{14}B$/Fe nanocomposite magnets to R&D of $Sm_2(Co,Fe)_{17}$ system.

Abstract

High-performance bulk anisotropic nanograin composite $Nd_2Fe_{14}B$/α-Fe and $Nd_2Fe_{14}B$/Fe-Co magnets were successfully synthesized using hot compacting blended Nd-Fe-B and α-Fe or Fe-Co powders or coated Nd-Fe-B powders followed by subsequent hot deformation. In the powder blending technique, melt-spun Nd-Fe-B powders that contain a minor Nd-rich phase are blended with a commercial α-Fe or Fe-Co powder; while in the powder coating technique, melt-spun Nd-Fe-B powders that contain a minor Nd-rich phase are coated with thin layers of α-Fe or Fe-Co. Using both techniques, $(BH)_{max}$ could reach 45 to 55 MGOe. The difference is that magnets prepared using the powder coating technique demonstrate significantly improved squareness of intrinsic demagnetization curves. Improved magnetic performance is anticipated with further advances in powder coating technologies.

Bulk anisotropic hybrid nanograin $Pr_2Fe_{14}B/PrCo_5$ magnets with improved thermal stability were synthesized. These magnets combine the high magnetic performance of $Pr_2Fe_{14}B$ and excellent thermal stability of $PrCo_5$ and can be used in applications in which the operating temperature and temperature coefficients of magnetic properties beyond Nd-Fe-B magnets are required.

Technologies developed in nanograin composite $Nd_2Fe_{14}B$/α-Fe magnets were used to make nanograin composite $Sm_2(Co,Fe)_{17}$/Fe-Co magnets. However, it has been observed that creating the desired crystallographic texture in $Sm_2(Co,Fe)_{17}$/Fe-Co is difficult. In addition, an interesting enhancement of magnetic performance was observed in a hot deformed $Sm(Co_{0.75}Fe_{0.11}Cu_{0.11}Zr_{0.03})_{7.3}$ magnet after heat treatment.

1. High-Performance Nanograin Composite $Nd_2Fe_{14}B/\alpha$-Fe and $Nd_2Fe_{14}B$/Fe-Co Magnets

1.1 Magnets prepared by using powder blending techniques

1.1.1 Magnets prepared by blending a melt-spun Nd-rich Nd-Fe-B powder and a commercial α-Fe or Fe-Co powder

It is well known that in order to obtain an anisotropic Nd-Fe-B magnet by hot deformation, it is critical to have a Nd-rich phase at grain boundaries in the magnet alloy. It is believed that at the hot deformation temperature (usually around 850 – 950°C), the Nd-rich phase is partially melted, which wets grain boundaries and facilitates the formation of the desired crystallographic texture [1]. However, no Nd-rich phase is present in a composite $Nd_2Fe_{14}B/\alpha$-Fe magnet alloy. Rather, a free α-Fe phase is present. Repeated experiments have demonstrated that it is difficult to obtain good grain alignment in composite $Nd_2Fe_{14}B/\alpha$-Fe magnet alloys without the Nd-rich phase.

Previously, bulk anisotropic nanocomposite $Nd_2Fe_{14}B/\alpha$-Fe magnets were made by hot compacting and hot deforming a mixture of two Nd-Fe-B powders, one with a Nd content slightly above the stoichiometric composition (11.76 at%) and the other with a Nd content below the stoichiometric composition. This technique is capable of producing nanocomposite $Nd_2Fe_{14}B/\alpha$-Fe magnets with $(BH)_{max}$ = 40 - 45 MGOe [2]. Experiments have established that improved magnetic performance can be obtained by substantially reducing the Nd content in the Nd-poor alloy. These results indicate that the best magnetic performance can be accomplished if the Nd content in the Nd-poor alloy is reduced to zero and, thus, the Nd-poor alloy becomes a pure α-Fe or Fe-B alloy.

The purity levels of the raw materials used in our experiments were Nd – 95%, Fe > 99%, Co > 99%, and Ga – 99.99 %. The composition of the Fe-B alloy was 20.54 wt% B; 77.72 wt% Fe. The particle size of the Fe powder was about 3 to 5 micrometers and the O_2 content was 0.2 wt%. The particle size of the 50%Fe-50%Co powder was about 10 to 50 micrometers. The Nd-Fe-Ga-B alloys were prepared by vacuum arc melting, followed by melt spinning with a wheel speed of 40 m/s. The ribbons were then crushed to 200 to 300 micrometers. Bulk magnet samples were prepared by a two-step process: RF inductive heating to 600 to 700°C, along with simultaneous compaction under a pressure of ~1.7 x 10^8 Pa for a total cycle time of ~2 minutes, followed by hot deformation (die upsetting) at 850 to 950°C under a pressure of ~6.9 x10^7 Pa for a total cycle time of 4 to 8 minutes. The typical sample height reduction in the latter step was 71%.

Samples were analyzed using a hysteresisgraph for room temperature magnetic properties, using a 13 mm diameter specimen. SEM, XRD and TEM were used to characterize particle size, grain alignment, and microstructures.

Figure 1.1 is a SEM micrograph showing α-Fe powder particles used in this research project. The powder particles are spheres and have an average diameter of 3 to 5 micrometers. Figure 1.2 shows the cross section of the α-Fe powder particles. It can be seen that the grain size of the α-Fe particles is in a nanometer range. Figure 1.3 shows Fe-Co particles used in this research project. Most Fe-Co particles have diameters ranging from 10 to 50 micrometers, although particles of only a few micrometers are also present. A SEM micrograph of a fracture surface of a Fe-Co particle is shown in Figure 1.4. Similar to the α-Fe particles, the Fe-Co particles also have nanograin structure. In order to make composite magnets, the α-Fe or Fe-Co powder was blended with the melt-spun Nd-rich Nd-Fe-B powder before hot compaction.

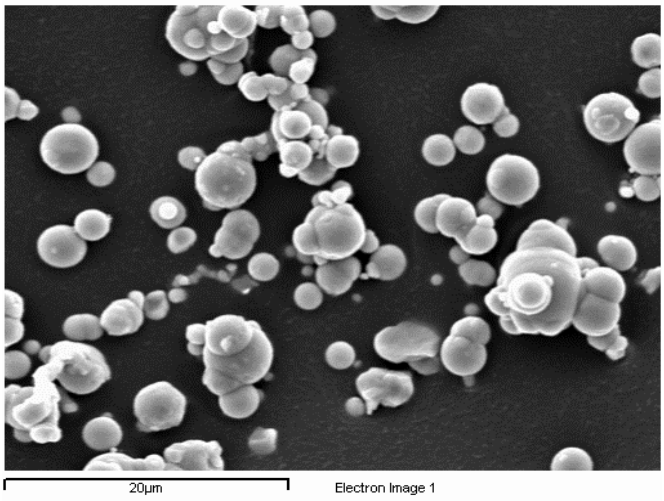

Fig. 1.1. α-Fe powder particles used in this project.

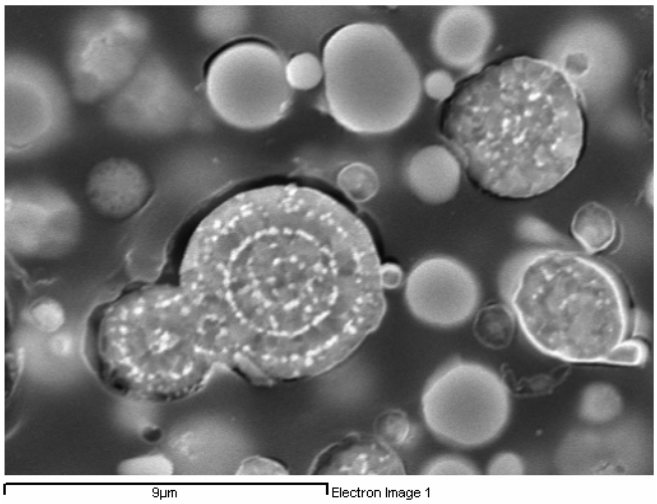

Fig. 1.2. Cross section of α-Fe powder particles.

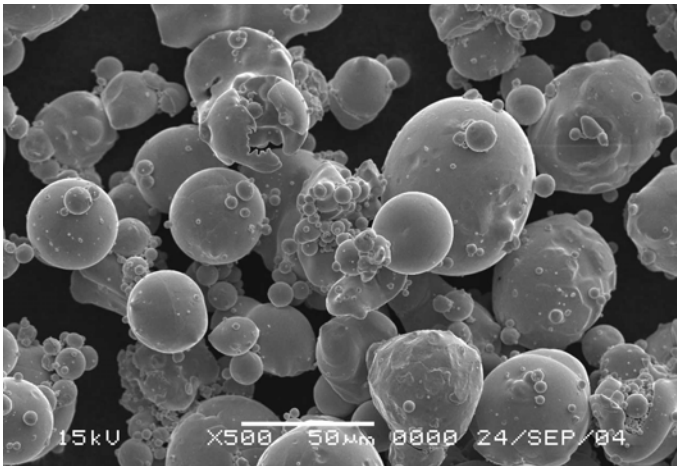

Fig. 1.3. Fe-Co powder particles used in this project.

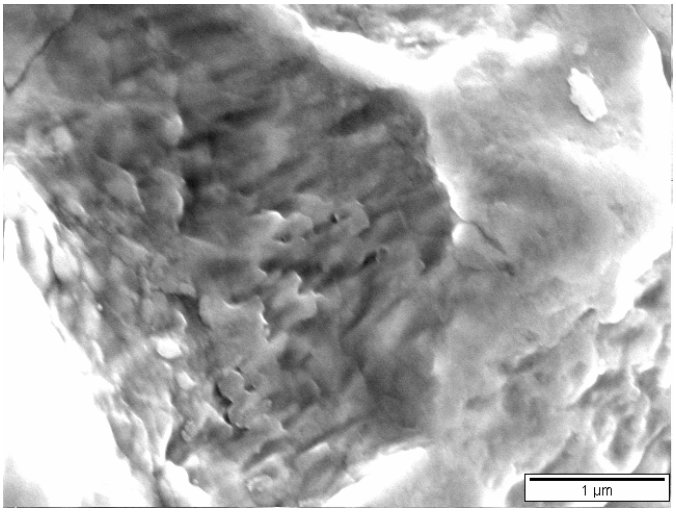

Fig. 1.4. SEM micrograph of a fracture surface of a Fe-Co particle.

Figure 1.5 is a SEM back-scattered electron image of a hot deformed $Nd_{13.5}Fe_{80}Ga_{0.5}B_6$/α-Fe (91.7 wt%/8.3 wt%) magnet. The dark gray phase is the α-Fe, while the light gray is the Nd-Fe-B phase. The α-Fe phase has length up to over 20 micrometers and thickness of 5 to 10 micrometers. Apparently, the α-Fe powder particles were agglomerated during processing.

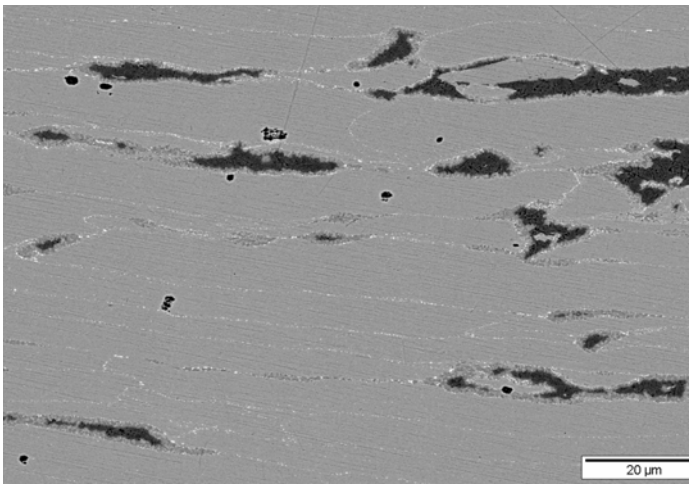

Fig. 1.5. SEM back-scattered electron image of a hot deformed composite $Nd_{13.5}Fe_{80}Ga_{0.5}B_6$/ α -Fe (91.7 wt%/8.3 wt%) magnet.

Unlike the α-Fe particles, the Fe-Co particles were not agglomerated. As shown in Figure 1.6, each individual Fe-Co phase (the dark gray phase) was formed from a single Fe-Co particle. Both composite $Nd_{14}Fe_{79.5}Ga_{0.5}B_6$/α-Fe and $Nd_{14}Fe_{79.5}Ga_{0.5}B_6$/Fe-Co magnets demonstrate smooth demagnetization curves with moderately high ${}_MH_c$ of over 10 kOe and $(BH)_{max}$ up to ~50 MGOe, as shown in Figures 1.7 and 1.8, respectively. The specimen as shown in Figure 1.6 has ${}_MH_c$ = 10.2 kOe and $(BH)_{max}$ = 46 MGOe. In comparison, the typical magnetic properties of the annealed $Nd_{14}Fe_{79.5}Ga_{0.5}B_6$ powder were $B_r \approx 8$ kG, ${}_MH_c \approx 17$ kOe, and $(BH)_{max} \approx 15$ MGOe.

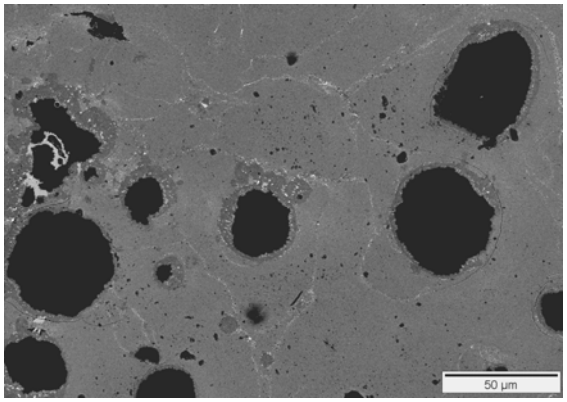

Fig. 1.6. SEM back-scattered electron image of a hot deformed composite $Nd_{14}Fe_{79.5}Ga_{0.5}B_6$/Fe-Co (95 wt%/5 wt%) magnet.

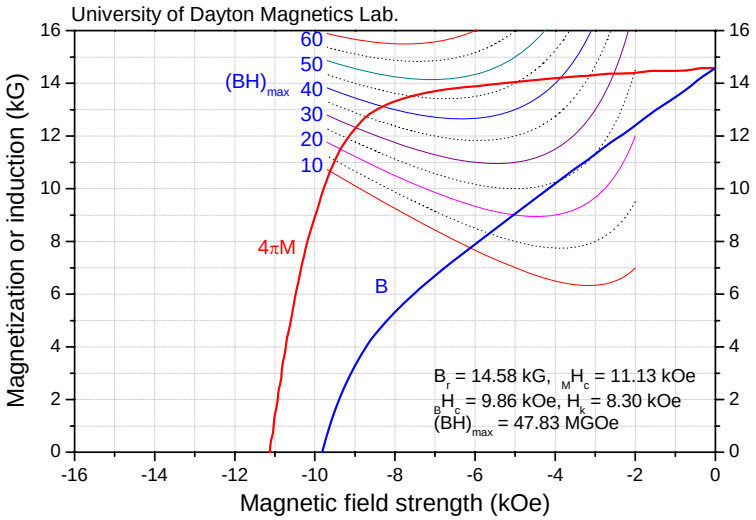

Fig. 1.7. Demagnetization curves of an anisotropic $Nd_{14}Fe_{79.5}Ga_{0.5}B_6$/α-Fe (95 wt%/5 wt%) magnet.

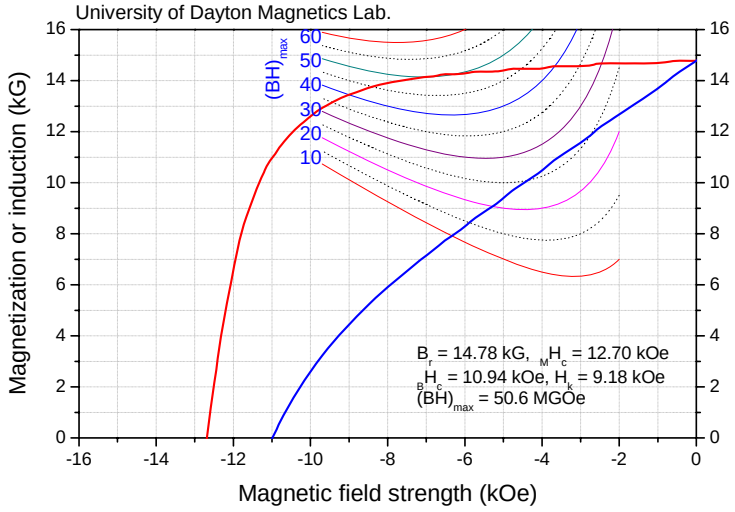

Fig. 1.8. Demagnetization curves of an anisotropic $Nd_{14}Fe_{79.5}Ga_{0.5}B_6$/Fe-Co (97 wt%/3 wt%) magnet.

Adding more soft phase resulted in higher magnetization but lower coercivity. The best magnetic performance was obtained when the α-Fe or Fe-Co fraction was around 3 to 8%. Figures 1.9 and 1.10 show the effects of the α-Fe fraction on the magnetic properties of composite $Nd_{14}Fe_{79.5}Ga_{0.5}B_6$/α-Fe magnets; Figures 1.11 and 1.12 show the effects of the Fe-Co fraction on the magnetic properties of composite $Nd_{14}Fe_{79.5}Ga_{0.5}B_6$/Fe-Co magnets. A small amount of Dy substituted for Nd in Nd-Fe-B led to substantial enhanced coercivity, which allowed adding additional soft phase in the composite magnets, while still maintaining acceptable magnetic properties. For example, a $Nd_{11}Dy_3Fe_{79.5}Ga_{0.5}B_6$/α-Fe magnet containing 15% α-Fe phase still demonstrates a high intrinsic coercivity value of over 10 kOe.

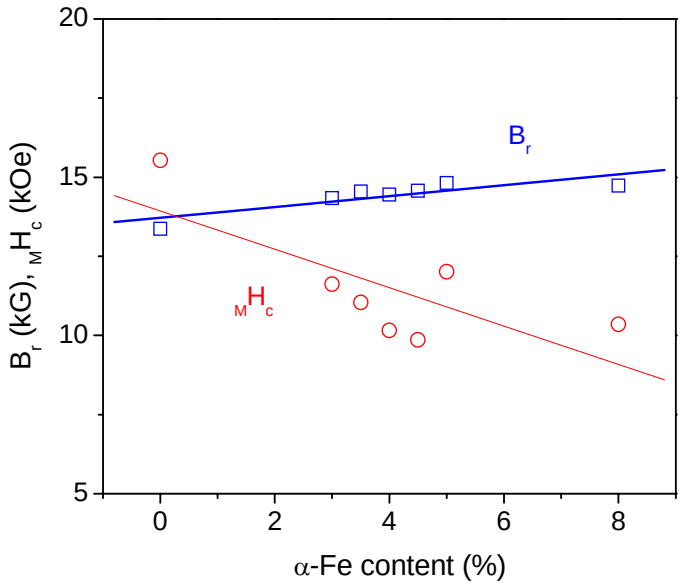

Fig. 1.9. Effects of the α-Fe content on B_r and $_MH_c$ of nanograin composite $Nd_{14}Fe_{79.5}Ga_{0.5}B_6$/α-Fe magnets.

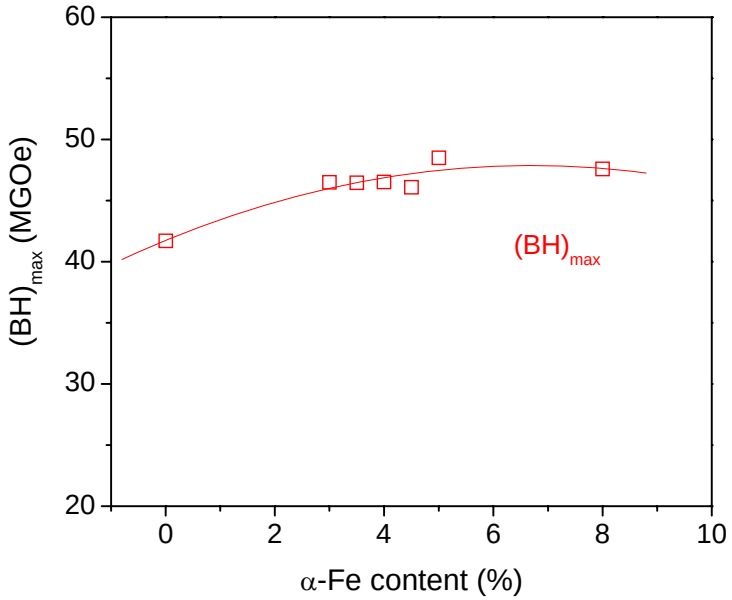

Fig. 1.10. Effects of the α-Fe content on $(BH)_{max}$ of nanograin composite $Nd_{14}Fe_{79.5}Ga_{0.5}B_6$/α-Fe magnets.

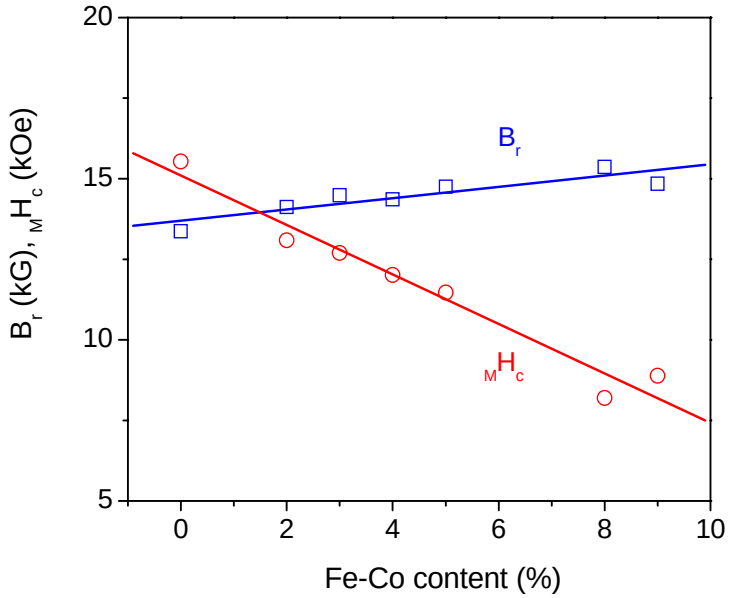

Fig. 1.11. Effects of Fe-Co fraction on B_r and $_MH_c$ of composite $Nd_{14}Fe_{79.5}Ga_{0.5}B_6$/Fe-Co magnets.

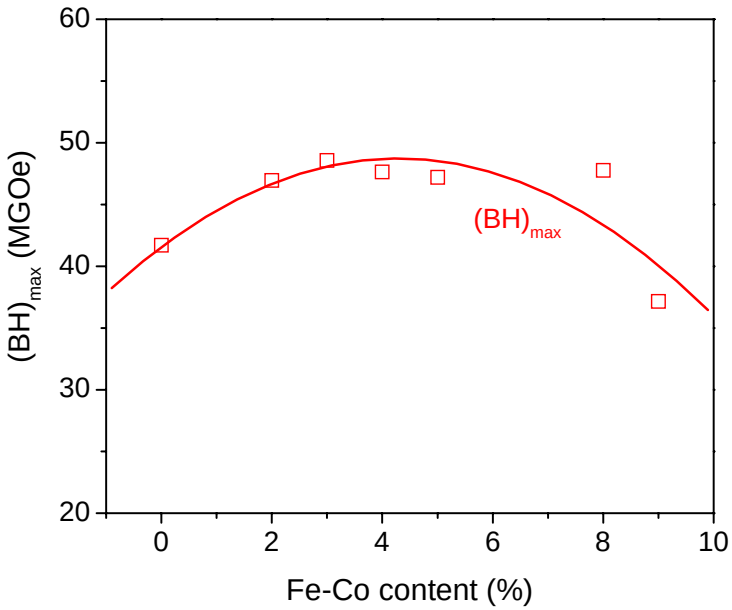

Fig. 1.12. Effects of Fe-Co fraction on $(BH)_{max}$ of composite $Nd_{14}Fe_{79.5}Ga_{0.5}B_6$/Fe-Co magnets.

Using the technique of blending Nd-Fe-B with α-Fe or Fe-Co powder can significantly improve grain alignment in composite magnets. Figure 1.13 compares XRD patterns of three magnets. Better grain alignment is represented by the enhanced (004), (006), and (008) intensity and a greater than 1 intensity ratio of (006) over (105). It can be seen that the grain alignment of the magnet prepared using the blending α-Fe technique is much better than that of a magnet prepared by blending a Nd-rich alloy and a Nd-poor alloy and similar to that of a commercial sintered anisotropic Nd-Fe-B magnet.

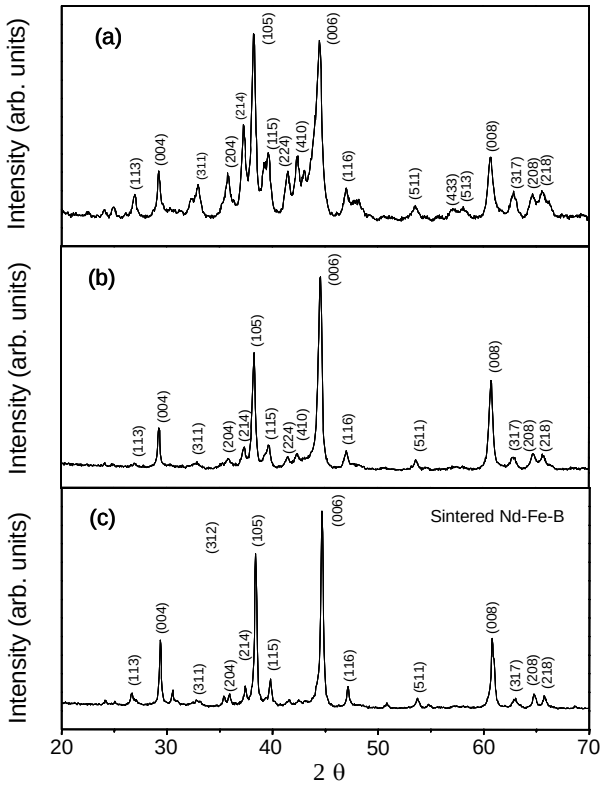

Fig. 1.13. Comparison of XRD patterns of (a) a composite $Nd_2Fe_{14}B/\alpha$-Fe magnet with $(BH)_{max}$ ~40 MGOe prepared by blending a Nd-rich Nd-Fe-B powder with a Nd-poor Nd-Fe-B powder, (b) a composite Nd-Fe-B/α -Fe magnet with $(BH)_{max}$ ~50 MGOe prepared by blending a Nd-rich Nd-Fe-B powder with an α-Fe powder, and (c) a commercial sintered Nd-Fe-B magnet with $(BH)_{max}$ ~40 MGOe.

Figure 1.14 shows elongated and aligned nanograins in the Nd-Fe-B matrix phase of a $Nd_{13.5}Fe_{80}Ga_{0.5}B_6/\alpha$-Fe (95 wt%/5 wt%) magnet with $(BH)_{max}$ = 48 MGOe. Figure 1.15 shows the hard/soft interface of the same specimen. In addition to elongated and aligned nano $Nd_2Fe_{14}B$ grains, large $Nd_2Fe_{14}B$ grains are usually observed at the interface, while large α-Fe particles basically maintain their original round shape after hot deformation.

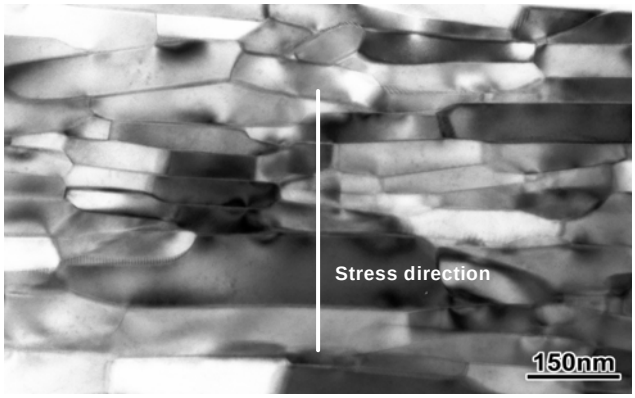

Fig. 1.14. A TEM micrograph of a $Nd_{13.5}Fe_{80}Ga_{0.5}B_6/\alpha$-Fe (95 wt%/5 wt%) magnet with $(BH)_{max}$ = 48 MGOe.

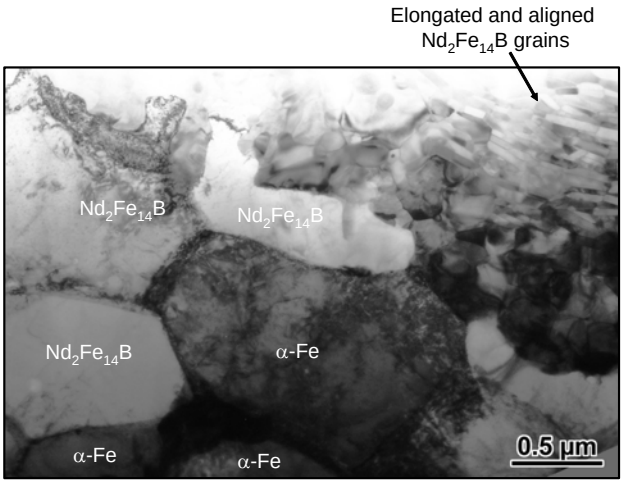

Fig. 1.15. A TEM micrograph of a composite $Nd_{13.5}Fe_{80}Ga_{0.5}B_6$/α-Fe (95 wt%/5 wt%) magnet showing hard/soft interface.

Previous studies [3-5] reported that the optimum soft phase size in a composite Nd-Fe-B/α-Fe magnet is ~10 nm and its upper limit is approximately 20 – 30 nm for effective interface exchange coupling. However, this study demonstrated that smooth demagnetization curves and high magnetic performance up to 50 MGOe can be obtained even when the soft phase is very large (up to ~40 micrometers). This soft phase dimension is more than 1000 times larger than the upper limit of the soft phase size suggested in the current models of interface exchange coupling. This indicates that the hard/soft interface exchange coupling in a composite magnet is actually much stronger than what investigators previously understood.

The microstructures shown in Figures 1-5 and 1-6 are by no means a desired microstructure. If the size of the soft phase could be significantly reduced and its distribution substantially improved, then more soft phase could be added into composite magnets without sacrificing coercivity, which would lead to a greatly enhanced $(BH)_{max}$.

1.1.2. Magnets prepared by using special powder blending techniques

Adding α-Fe or Fe-Co into Nd-Fe-B magnet material certainly enhances the saturation magnetization, but reduces coercivity. The magnitude of the coercivity reduction is dependent not only on the amount of α-Fe or Fe-Co added, but also on its particle size and particle distribution. It is easy to understand that fine α-Fe or Fe-Co particles and dispersed distribution of the soft phase in the hard Nd-Fe-B matrix increases the hard/soft interface area and, thus, enhances the interaction between hard and soft phases, which will minimize the coercivity loss.

The above-mentioned composite magnets were prepared by using a mechanical blending method to mix two powders. SEM observation shows that the soft phase in composite magnets synthesized using mechanical blending is very large (up to around 40 micrometers). In order to improve the soft phase distribution, the effects of ultrasonic blending and a ball milling blending were investigated. In the ultrasonic blending, the melt-spun Nd-Fe-B powder is first blended mechanically with 4 wt%, 6 wt%, a 10 wt% of commercial a-Fe powder. Then the powder mixtures are subjected to ultrasonic vibration. In the ball milling blending, melt-spun Nd-Fe-B powder and α-Fe powder are blended and ball-milled for 20, 40 and 60 minutes, respectively. However, no improvement in the soft phase distribution and magnetic properties was observed.

1.1.3 Magnets prepared by blending Nd-Fe-B powder with α-Fe nanoparticles

The effect of utilizing α-Fe nanoparticles was investigated. The α-Fe nanoparticles used in this experiment were obtained from CMU and were agglomerated as small pieces 1 to 3 mm in size. Before powder blending, these α-Fe pieces were first annealed at 540°C for 8.5 hours in a H_2 atmosphere. After the anneal, the small α-Fe pieces were manually crushed into fine powder in a glove box under an argon atmosphere. The fine α-Fe powder was then blended with $Nd_2Fe_{14}B$ powder with the fraction of the α-Fe powder to be 4 wt%. The hot compaction was performed at 600°C and hot deformation at 960°C for about 5 minutes with 71% height reduction.

No improvement in magnetic properties was achieved by using α-Fe nanoparticles. Figure 1.16 shows a SEM backscattered electron image of the $Nd_2Fe_{14}B$/α-Fe [96 wt%/4 wt%] magnet specimen, characterized as quite large α-Fe phase. The length of the α-Fe phase is up to 60 micrometers while its thickness is about 10 micrometers. Apparently, most α-Fe exists in the nanocomposite magnet as a very large phase, rather than very small dispersed phase as expected. In addition, five different zones exist in the microstructure of the nanocomposite magnet. As shown in Figure 1.16, Zone 1 is the $Nd_2Fe_{14}B$ matrix phase, Zone 2 is the pure α-Fe part in the α-Fe phase, Zone 3 is a diffusion area between the $Nd_2Fe_{14}B$ and α-Fe phases, and Zone 4 is a phase rich in oxygen that is most likely introduced from the oxide layer on the α-Fe surface. In addition, another oxygen-rich phase exists in the magnet as shown in Zone 5 in Figure 1.16. This phase is introduced from the oxide layer on the surface of Nd-Fe-B flakes.

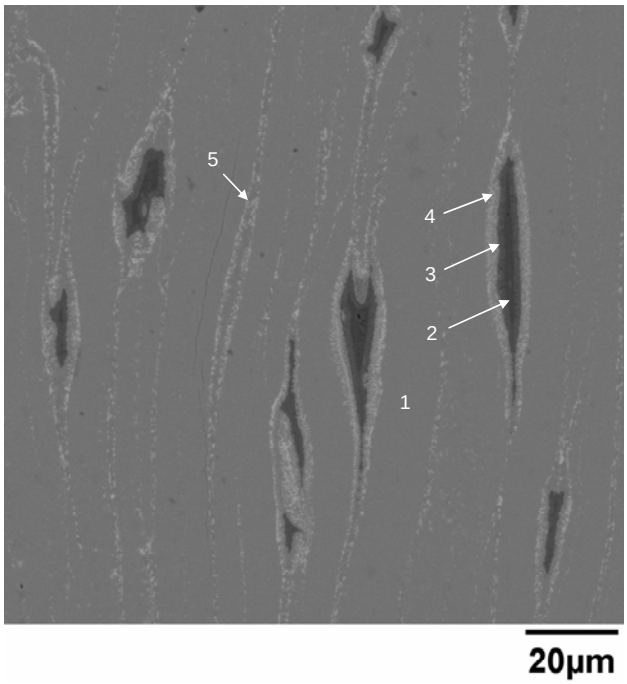

Fig. 1.16. SEM backscattered electron image of the $Nd_2Fe_{14}B$/α-Fe (96 wt%/4 wt%) magnet specimen.

1.1.4 Magnets prepared by blending Nd-Fe-B powder with Fe-Co-B ribbons

Nanograin composite $Nd_2Fe_{14}B/Fe_{50}Co_{49}B$ magnets were prepared by blending melt spun $Nd_2Fe_{14}B$ ribbons with melt spun $Fe_{50}Co_{49}B$ ribbons. The $Fe_{49.5}Co_{49.5}B$ alloy was melted using an arc melting furnace and, subsequently, melt spun with 40 m/s at WPAFB. The purpose of adding a small amount of B into the Fe-Co alloy is to increase its brittleness. It was observed that after melt spinning, the $Fe_{49.5}Co_{49.5}B$ ribbons are more brittle than the pure Fe-Co alloy.

After blending 7 wt% $Fe_{49.5}Co_{49.5}B$ with $Nd_2Fe_{14}B$ ribbons, the powder mixture was hot compacted at 560°C for a total of 2 minutes under 25 kpsi, followed by hot deformation at 950°C for 5 minutes under around 10 kpsi with 71% deformation. After hot deformation, the specimen was characterized at room temperature using a hysteresisgraph. Again, magnetic properties obtained were relatively poor and are believed to be caused by the large dimension of the $Fe_{49.5}Co_{49.5}B$ ribbons.

1.2 Magnets prepared by using coating technologies

In order to significantly decrease the size and improve the distribution of the soft phase, a new approach was applied to make nanograin composite magnets by coating the melt-spun Nd-Fe-B powder particles with thin layers of α-Fe or Fe-Co followed by normal hot compaction and hot deformation. In this research project, various coating techniques were investigated, including DC and RF sputtering, pulsed laser deposition (PLD), chemical (electroless) coating, and electrolytic coating. The coated powders were hot compacted at 550 to 650°C under 1.7×10^8 Pa for a total cycle time of about 2 minutes using a hot press with inductive heating, followed by die upsetting at 850 to 950°C under around 6.9×10^7 Pa for 4 to 8 minutes with a height reduction of 70%.

SEM/EDS was used to observed and analyze the coated powder particles. SEM and TEM were used to observe microstructures of the nanograin composite magnets. X-ray diffraction was used to analyze grain alignment and a hysteresisgraph was used to characterize room temperature magnetic properties of bulk composite magnets. In addition, the oxygen contents of the coated powders were analyzed following LECO ISO 9001 procedures.

Among the various coating technologies used, chemical coating demonstrated the lowest deposition rate, while electrolytic coating showed the highest. On the other hand, sputtering, PLD, and chemical coating are associated with the lowest oxygen pickup. Using these methods, only 0.04 to 0.06 wt% oxygen was detected -- very close to the original oxygen content of uncoated powders. Electrolytic coating had the highest oxygen pickup, with oxygen content in the range of 0.1 to 0.3 wt%.

Using the various coating technologies, the bulk anisotropic Nd-Fe-B/Fe-Co composite magnets reached $(BH)_{max}$ = 45 – 55 MGOe with significantly improved squareness of demagnetization curves, as compared with composite magnets prepared by just blending powders. The electrolytic coating resulted in thick coated layers; however, the corresponding $(BH)_{max}$ values were less than 50 MGOe due to significant oxygen pickup during processing. Detailed information for nanograin composite magnets prepared using various coating techniques are provided in the following paragraphs.

1.2.1 Magnets prepared by using DC and RF sputtering techniques

Both DC and RF sputtering techniques were used to coat Nd-Fe-B powders. The target used was an α-Fe metal or an Fe-Co-V alloy (Hiperco 50). A rotating powder sample hold was used to obtain more uniform coated layers. The sputtering was performed under Ar atmosphere with the chamber pressure of 15 mtorr.

The SEM observations showed that in most cases, the coated layers were not smooth and uniform, but had rough and mottled morphology as shown in Figures 1.17 and 1.18. Figure 1.19 is a SEM/EDS of a coated surface of a Nd-Fe-B powder particle when a Fe-Co-V target was used for sputtering. The vanadium peaks in the EDS clearly demonstrate the existence of the coated layer.

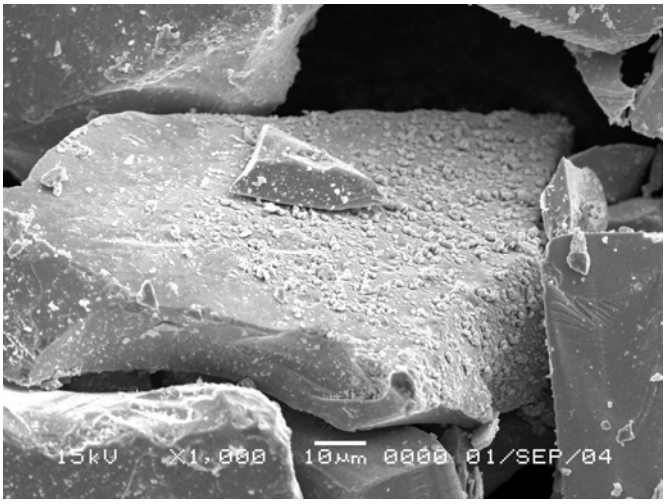

Fig. 1.17. A SEM micrograph of Nd-Fe-B powder particles after DC sputtering.

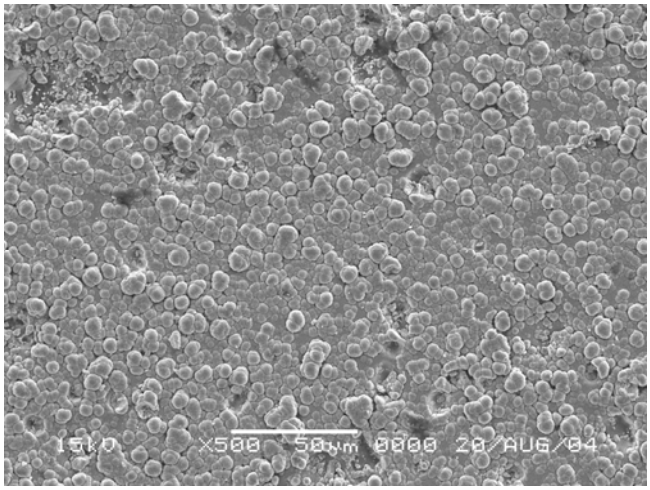

Fig. 1.18. A SEM micrograph of a coated surface of a Nd-Fe-B powder particle after DC sputtering.

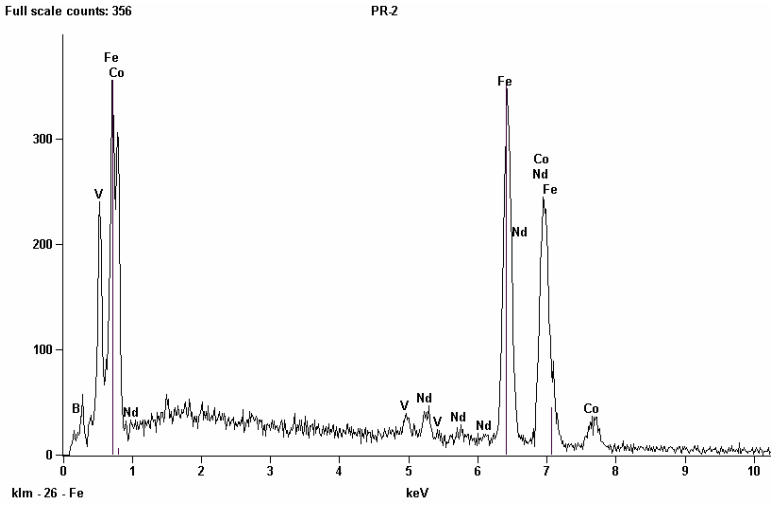

Fig. 1.19. SEM/EDS of a coated surface of Nd-Fe-B powder particle.

Nanograin composite magnets prepared using the sputtering technique demonstrated increased intrinsic coercivity and significantly improved loop squareness as specified by the knee field value. Figures 1.20 and 1.21 show demagnetization curves of nanograin composite $Nd_{14}Fe_{79.5}Ga_{0.5}B_6$/Fe-Co magnets prepared using DC sputtering for 8 and 21 hours, respectively.

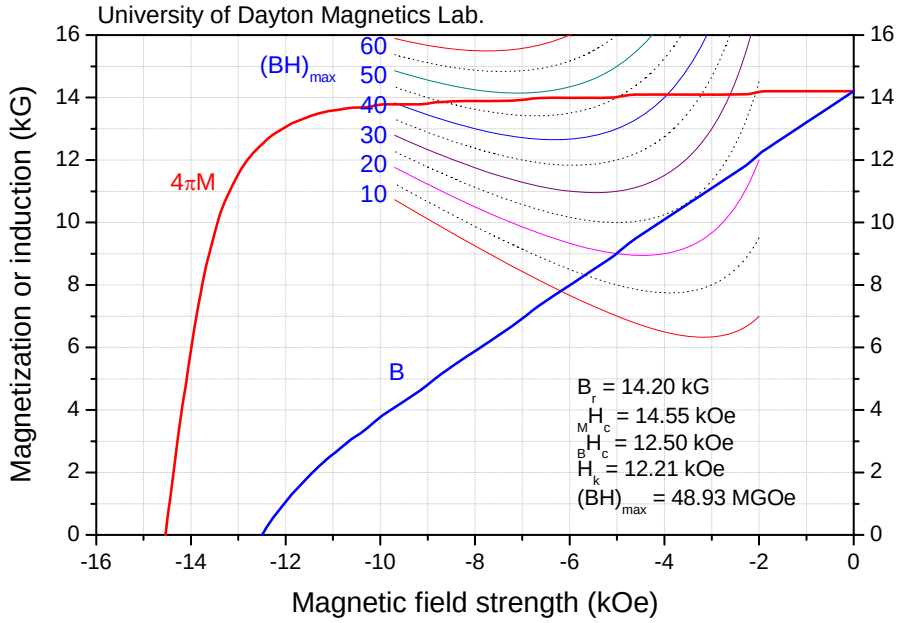

Fig. 1.20. Demagnetization curves of a composite $Nd_{14}Fe_{79.5}Ga_{0.5}B_6$/Fe-Co magnet prepared using DC sputtering for 8 hours.

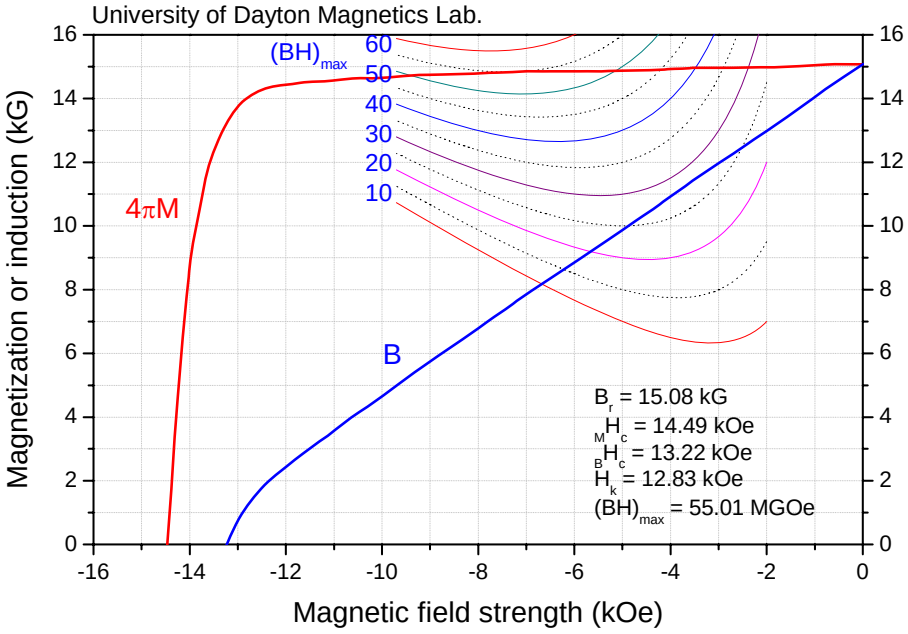

Fig. 1.21. Demagnetization curves of a composite $Nd_{14}Fe_{79.5}Ga_{0.5}B_6$/Fe-Co magnet prepared using DC sputtering for 21 hours.

1.2.2 Magnets prepared by using PLD technique

Nanograin composite Nd-Fe-B/Fe-Co magnets were synthesized by compacting melt-spun Nd-Fe-B powders coated with thin Fe-Co layers followed by hot deformation. The target for PLD was a Fe-Co-V alloy (Hiperco 50). The laser used was Nd:YAG (1064 nm), at 340 mJ/pulse and 10 Hz. The chamber pressure was 10^{-7} torr. The PLD time varied from 15 minutes up to 20 hours. Similar to sputtering, one advantage of PLD is its very low oxygen pickup during the process. In this study, three specimens collected from the PLD coated powder sample were sent to LECO for oxygen analyses and the results were 0.0437, 0.0438, and 0.0453 wt%. These values are in the same oxygen level as the original melt-spun powders (0.04 to 0.05 wt%).

Magnetic performance of nanograin composite Nd-Fe-B/Fe-Co magnets prepared by compacting PLD powders followed by hot deformation is similar to that of magnets prepared by using sputtering technique. $(BH)_{max}$ values of around 45 to 55 MGOe can be reached. Figure 1.22 shows demagnetization curves of a composite $Nd_{14}Fe_{79.5}Ga_{0.5}B_6$/Fe-Co magnet prepared using PLD for 6 hours. Similar to sputtering, extending the deposition time beyond 10 hours led to no significant improvement in magnetic performance.

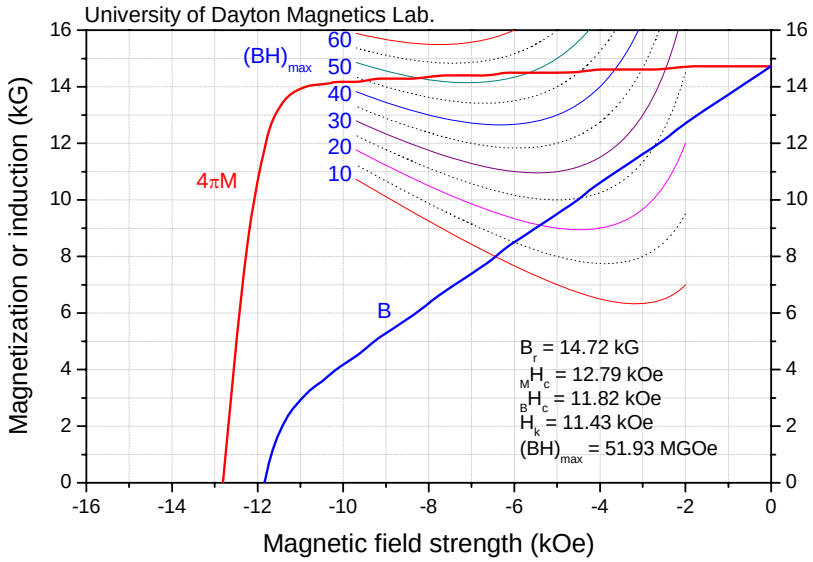

Fig. 1.22. Demagnetization curves of a composite $Nd_{14}Fe_{79.5}Ga_{0.5}B_6$/Fe-Co magnet prepared using PLD for 6 hours.

1.2.3 Magnets prepared by using chemical coating technique

Both sputtering and PLD are time consuming processes with high cost. In order to find a more cost-effective deposition approach, we investigated a chemical (electroless) coating technique to coat Nd-Fe-B powders with thin Fe-Co layers. Compared with sputtering or PLD, the advantages of chemical coating include: (1) more process parameters are controllable, such as coating solution concentration, coating temperature, and coating time; (2) coating time is significantly reduced; and (3) the cost is much lower.

The chemical coating process parameters are listed below:

- Chemicals: $FeCl_2$, $CoCl_2$, or $FeSO_4$, $CoSO_4$
- Reducing agent: NaH_2PO_2
- Complexing agent: $Na_3C_6H_5O_7$
- pH value: 5 to 8

- Temperature: 20 to 50°C
- Time: 15 minutes to 3 hours

Figures 1.23 and 1.24 shows demagnetization curves of $Nd_{14}Fe_{79.5}Ga_{0.5}B_6$/Fe-Co magnets prepared using chemical coating at room temperature for 1 hour.

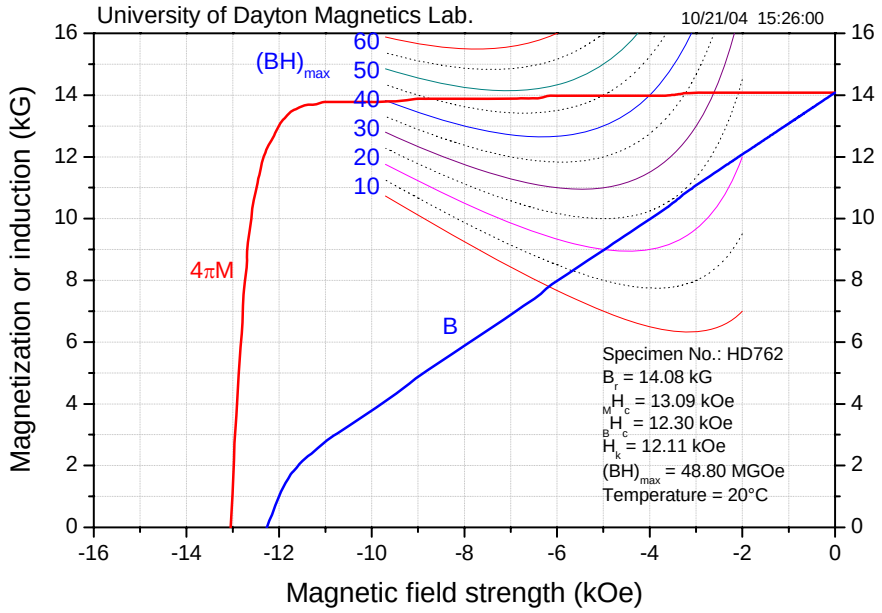

Fig. 1.23. Demagnetization curves of a composite $Nd_{14}Fe_{79.5}Ga_{0.5}B_6$/Fe-Co magnet prepared using chemical coating for 1 hour with $(BH)_{max}$ = 48.8 MGOe.

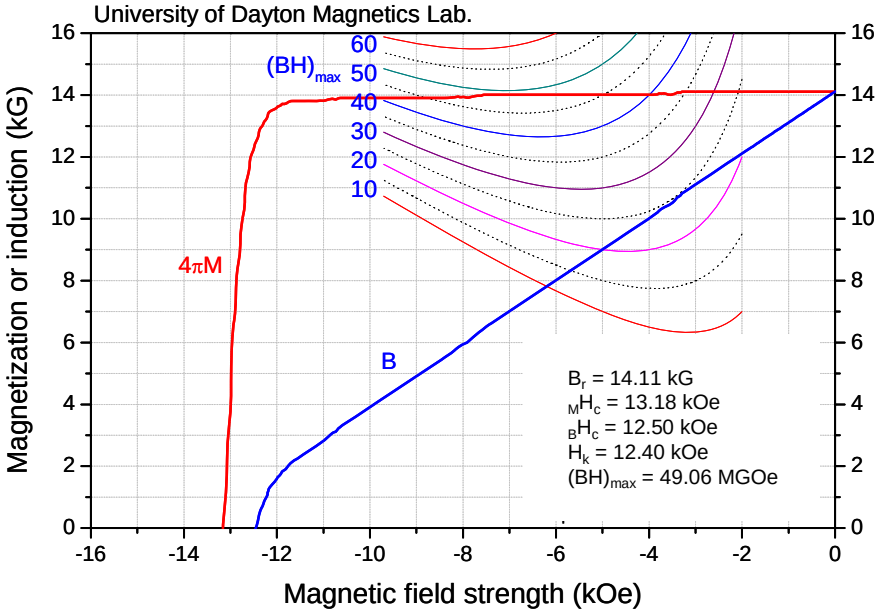

Fig. 1.24. Demagnetization curves of a composite $Nd_{14}Fe_{79.5}Ga_{0.5}B_6$/Fe-Co magnet prepared using chemical coating for 1 hour with $(BH)_{max}$ = 49.06 MGOe.

1.2.4 Magnets prepared using electrolyte coating technique

It was observed that the deposition rate of the chemical Fe-Co or α-Fe coating is slow. Further, only one-fourth to one-third of the powder particles could be coated with Fe-Co or α-Fe layers. Most powder particles could not be coated with any soft magnetic material. To significantly increase the coating rate, the feasibility of applying electrolyte coating was investigated.

The apparatus used for electrolyte coating is shown in Figure 1.25. The electrolyte coating process parameters are listed below:

- Anode: α-Fe or Fe-Co-V (Hiperco 50)
- Cathode: Al
- Chemicals: $FeCl_2$, $CoCl_2$, or $FeSO_4$, $CoSO_4$
- Additions:
  - $MnCl_2.4H_2O$
  - H_3BO_3
- pH value: 2 to 3
- Temperature: 25 to 30°C
- Time: 0.5 to 2 hrs
- Cathode current density: 0.5 to 5 A/dm^2

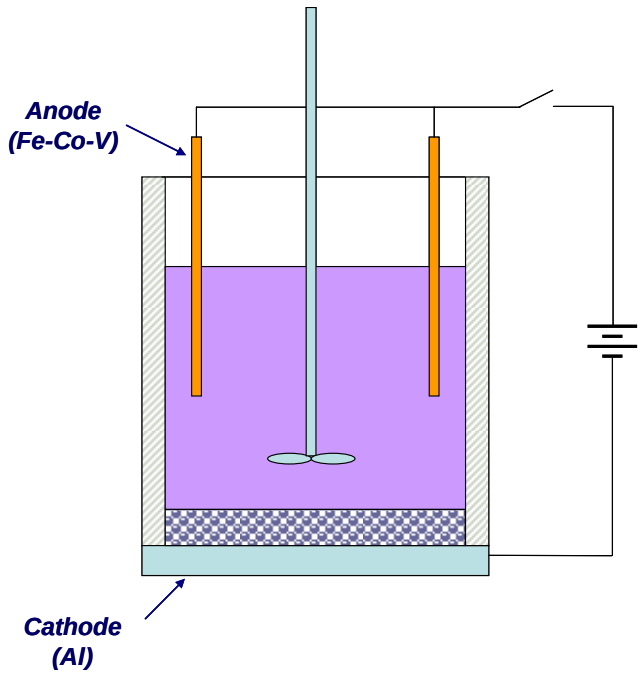

Fig. 1.25. Apparatus for electrolyte coating.

Figure 1.26 shows SEM micrographs of the surfaces of Nd-Fe-B particles coated using electrolyte coating with different magnifications. From the morphology of the coated Fe-Co-V at high magnification, such as Figure 1.26 (d), it is believed that the coated Fe-Co-V is in an amorphous condition. Figure 1.27 shows SEM/EDS of the surface of a Nd-Fe-B particle coated using electrolyte coating. The peaks of vanadium in the EDS clearly demonstrate the existence of the coated layer.

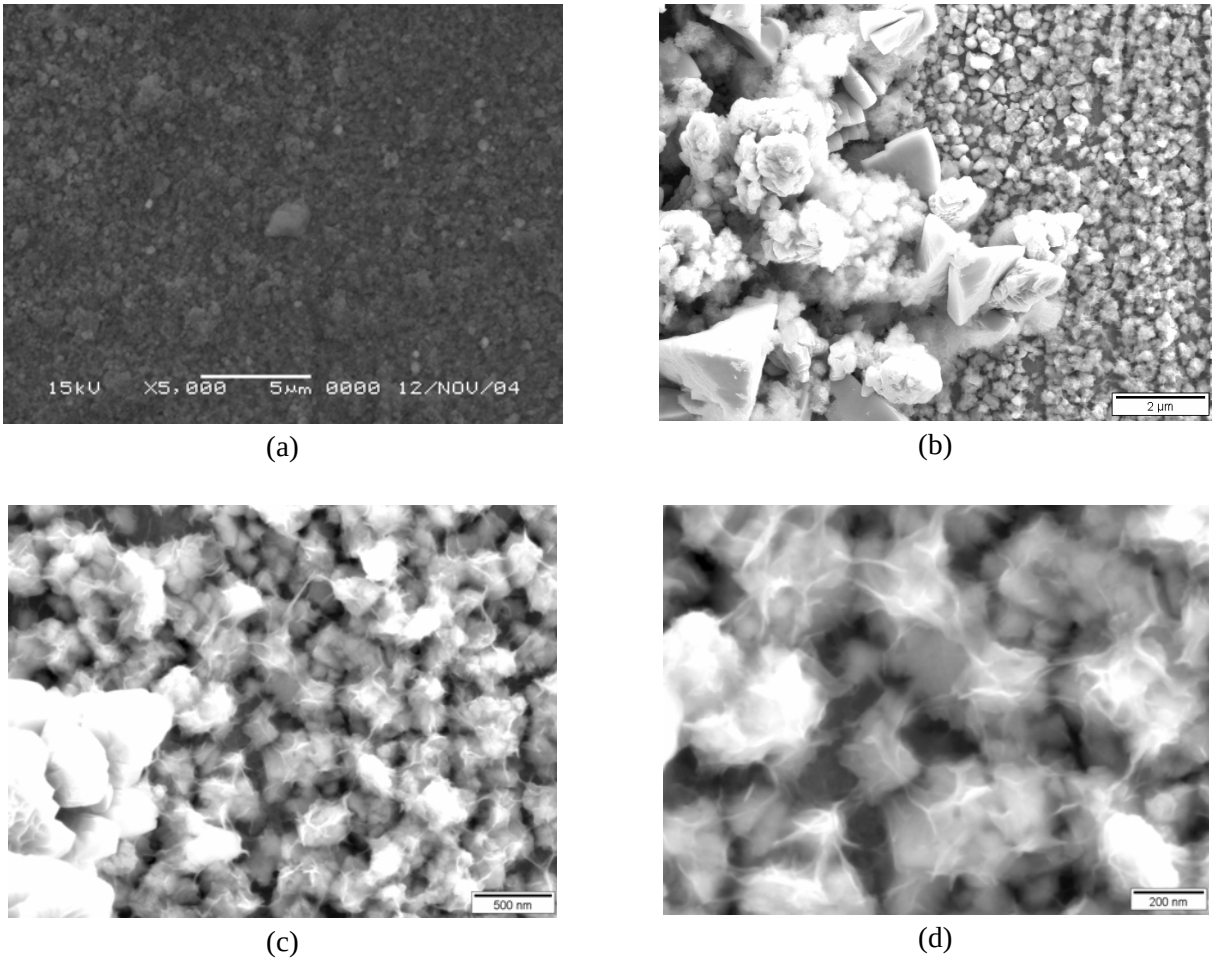

(a) (b)

(c) (d)

Fig. 1.26. SEM micrographs of the surfaces of Nd-Fe-B particles coated using electrolyte coating with different magnifications.

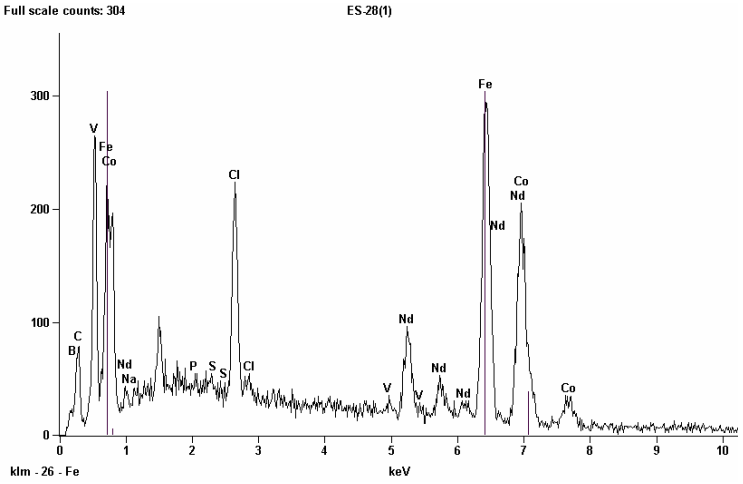

Fig. 1.27. SEM/EDS of the surface of a Nd-Fe-B particle coated using electrolyte coating.

Figure 1.28 illustrates demagnetization curves of a composite $Nd_{14}Fe_{79.5}Ga_{0.5}B_6$/a-Fe magnet prepared using electrolyte coating for 30 minutes under 2 volts and 1 ampere. Because magnets prepared using electrolyte coating have a relatively high oxygen content ranging 0.1 to 0.3 wt%, these magnets demonstrate relatively low ${}_MH_c$ and $(BH)_{max}$.

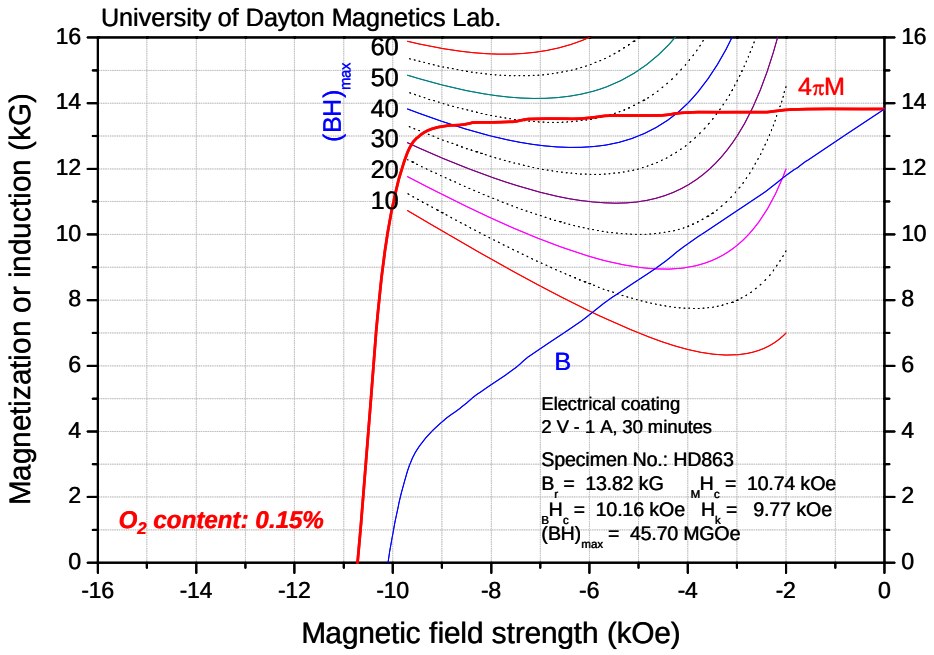

Fig. 1.28. Demagnetization curves of a composite $Nd_{14}Fe_{79.5}Ga_{0.5}B_6$/α-Fe magnet prepared using electrolyte coating for 30 minutes.

Figure 1.29 shows a SEM micrograph of a composite $Nd_{14}Fe_{79.5}Ga_{0.5}B_6$/α-Fe magnet prepared using electrolyte coating. In addition to the matrix Nd-Fe-B phase, the corresponding EDS (Figure 1.30) identified a α-Fe phase (the black phase in Figure 1.29) and a Nd- and oxygen-rich phase (the white phase in Figure 1.29).

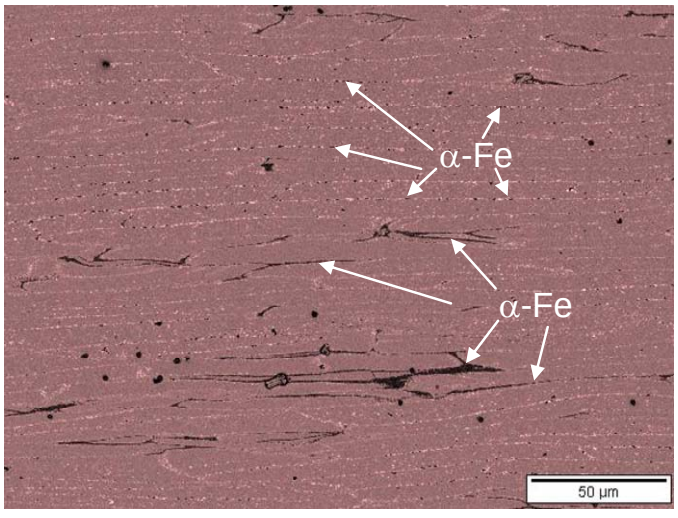

Fig. 1.29. SEM micrograph of a composite $Nd_{14}Fe_{79.5}Ga_{0.5}B_6$/α-Fe magnet prepared using electrolyte coating.

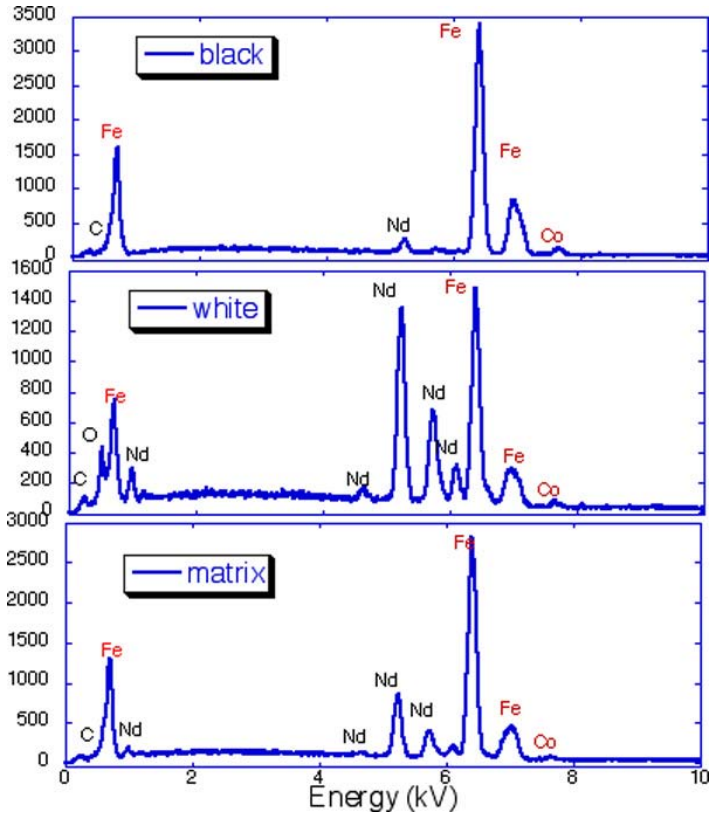

Fig. 1.30. SEM/EDS of a composite $Nd_{14}Fe_{79.5}Ga_{0.5}B_6$/Fe magnet prepared using electrolyte coating.

Figure 1.31 shows a TEM micrograph of the matrix phase of a $Nd_{14}Fe_{79.5}Ga_{0.5}B_6$/α-Fe magnet prepared using electrolyte coating, demonstrating elongated and aligned Nd-Fe-B grains. Figure 1.32 is a TEM micrograph of a $Nd_{14}Fe_{79.5}Ga_{0.5}B_6$/α-Fe magnet prepared using electrolyte coating, showing Nd-Fe-B grains and a minor Nd-rich phase.

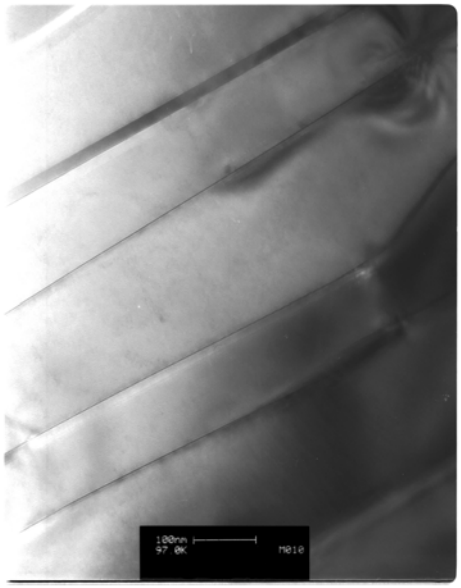

Fig. 1.31. TEM micrograph of a $Nd_{14}Fe_{79.5}Ga_{0.5}B_6$/α-Fe magnet prepared using electrolyte coating.

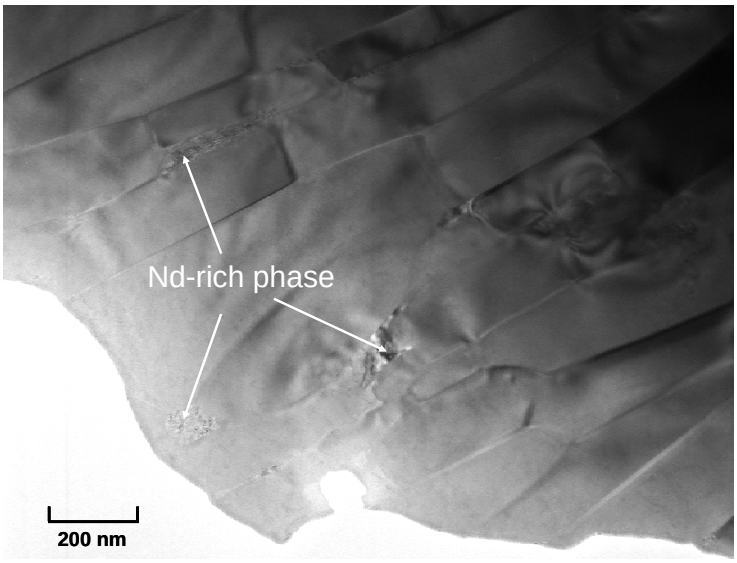

Fig. 1.32. TEM micrograph of a $Nd_{14}Fe_{79.5}Ga_{0.5}B_6$/α-Fe magnet prepared using electrolyte coating, showing Nd-Fe-B grains and a minor Nd-rich phase.

It has been observed that nanograin composite magnets prepared using electrolyte coating demonstrate significantly improved squareness of demagnetization curves as a result of improved grain alignment. Table 1-1 compares the ratios of H_k over ${}_MH_c$ and $4\pi M$ at $(BH)_{max}$ over $(4\pi M)_{max}$ of various magnets including (1) hot compacted and hot deformed Nd-Fe-B with commercial composition (without soft phase); (2) nanograin composite Nd-Fe-B/α-Fe synthesized by blending with α-Fe powder; (3) nanograin composite Nd-Fe-B/α-Fe synthesized by sputtering; and (4) nanograin composite Nd-Fe-B/α-Fe synthesized by chemical coating. Apparently, composite Nd-Fe-B/α-Fe magnets synthesized by blending with α-Fe powder demonstrate the worst squareness of the demagnetization curves; while composite Nd-Fe-B/α-Fe magnets synthesized by chemical coating show the best squareness of the demagnetization curves.

Table 1-1. Comparison of Grain Alignment Represented by $H_k/{}_MH_c$ and $4\pi M$ at $(BH)_{max}/(4\pi M)_{max}$

Materials	H_k / ${}_MH_c$ (%)	$4\pi M$ at $(BH)_{max}$ / $(4\pi M)_{max}$ (%)	Note
Hot compacted and hot deformed Nd-Fe-B with commercial composition (without soft phase)	96.0	85.4	Average of 10 specimens
Nano grain composite Nd-Fe-B/α-Fe synthesized by blending with α-Fe powder	93.7	78.8	Average of 10 specimens
Nanograin composite Nd-Fe-B/α-Fe synthesized by sputtering	96.7	88.5	Average of 10 specimens
Nanograin composite Nd-Fe-B/α-Fe synthesized by chemical coating	97.7	89.1	Average of 10 specimens

1.2.5 Effect of original particle size

In this research project, we investigated the effect of the powder particle size of the original melt-spun $Nd_2Fe_{14}B$ powder particles on magnetic properties of composite $Nd_2Fe_{14}B$/Fe-Co magnets prepared using electric coating and chemical coating followed by normal RF inductive hot compaction and hot deformation.

Previous preliminary experiments indicated that using $Nd_2Fe_{14}B$ fine powder particles often leads to relatively lower coercivity. However, when powder coating is involved, finer powder particles have larger total surface areas, which means that for the same thickness of coating layers, a larger fraction of the magnetically soft phase can be obtained. Therefore, it is necessary to study the effect of the original powder particle size on magnetic properties of composite $Nd_2Fe_{14}B$/Fe-Co magnets prepared using coating technologies.

Table 1-2 summarizes the results of this study. Generally speaking, composite magnets prepared using powder particles with intermediate sizes (-80+140 mesh) demonstrate higher intrinsic coercivity and slightly better $(BH)_{max}$. The highest intrinsic coercivity value of 14.48 kOe was obtained in a magnet made from (-80+140 mesh) powder, while high energy product values of 44.6 and 44.0 MGOe were obtained in magnets made from coarse powder (+80 mesh) and intermediate size powder (-80+140 mesh), respectively.

Demagnetization curves of a few selected composite magnets are given in Figures 1.33 through 1.35. It is apparent that all magnets show very good squareness of demagnetization curves.

Table 1-2. Effect of Original Nd-Fe-B Particle Size on Magnetic Properties of Composite Nd-Fe-B/Fe-Co Magnets Preparing Using Different Coating Techniques

	Particle size (mesh)		
	+ 80	-80+140	-140
Electric coating	HD1591 B_r = 12.64 kG $_MH_c$ = 12.15 kOe $(BH)_{max}$ = 38.37 MGOe	HD1594 B_r = 13.16 kG $_MH_c$ = 13.02 kOe $(BH)_{max}$ = 41.36 MGOe	
		HD1595 B_r = 13.38 kG $_MH_c$ = 13.02 kOe $(BH)_{max}$ = 43.42 MGOe	
Chemical coating	HD1606 B_r = 13.56 kG $_MH_c$ = 12.53 kOe $(BH)_{max}$ = 44.6 MGOe	HD1597 B_r = 13.46 kG $_MH_c$ = 14.48 kOe $(BH)_{max}$ = 44.0 MGOe	HD1604 B_r = 13.06 kG $_MH_c$ = 12.05 kOe $(BH)_{max}$ = 40.72 MGOe
	HD1608 B_r = 13.08 kG $_MH_c$ = 12.24 kOe $(BH)_{max}$ = 40.99 MGOe	HD1601 B_r = 13.34 kG $_MH_c$ = 13.99 kOe $(BH)_{max}$ = 43.05 MGOe	HD1605 B_r = 12.96 kG $_MH_c$ = 11.56 kOe $(BH)_{max}$ = 40.66 MGOe

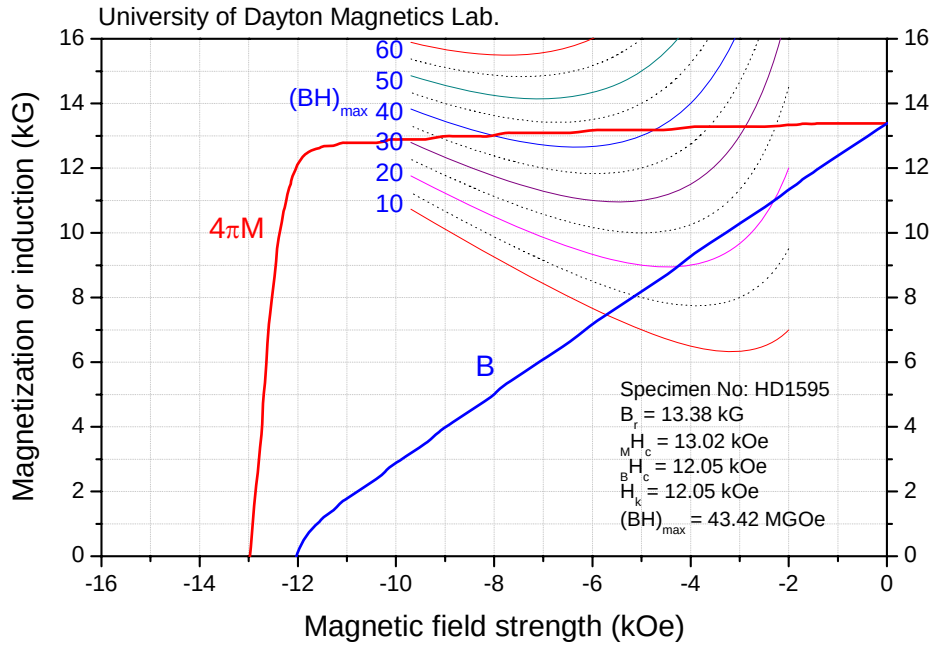

Fig. 1.33. Demagnetization curves of hot deformed $Nd_2Fe_{14}B$/Fe-Co magnet prepared using electric coating with powder particle size of -80+140 mesh.

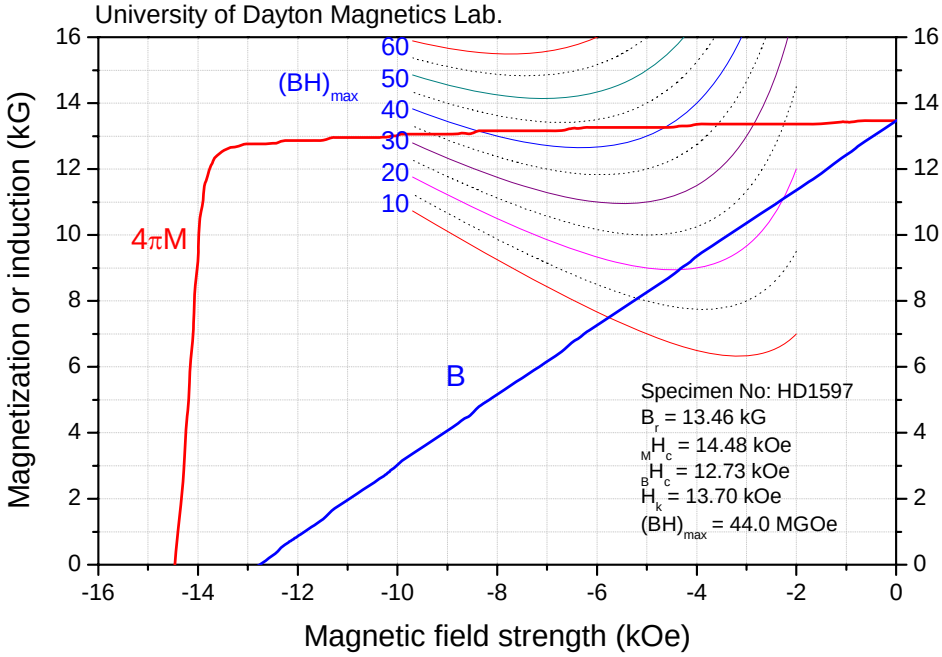

Fig. 1.34. Demagnetization curves of hot deformed $Nd_2Fe_{14}B$/Fe-Co magnet prepared using chemical coating with powder particle size of -80+140 mesh.

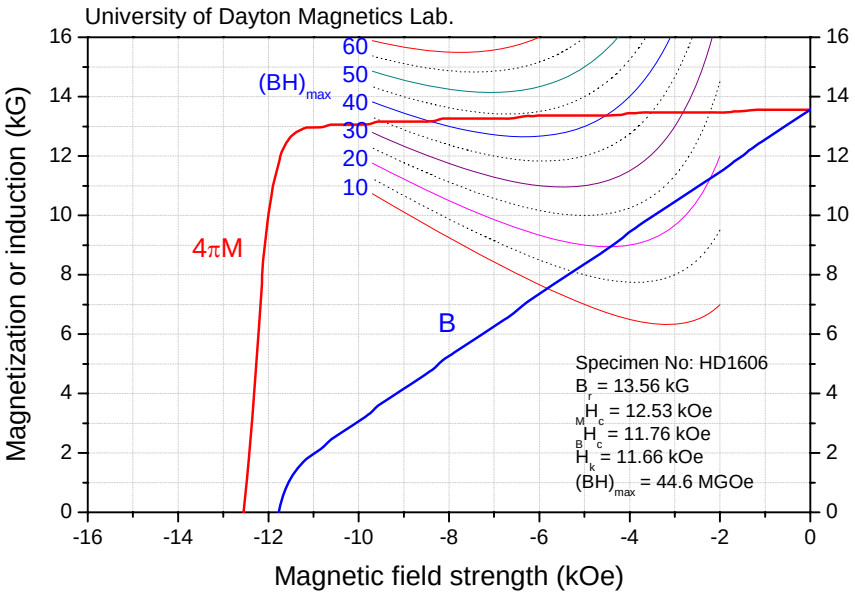

Fig. 1.35. Demagnetization curves of hot deformed $Nd_2Fe_{14}B$/Fe-Co magnet prepared using chemical coating with powder particle size of +80mesh.

1.2.6 Effect of hot deformation temperature

Magnetic properties of nanocomposite $Nd_2Fe_{14}B/\alpha$-Fe magnet are strongly dependent on processing parameters, especially hot compaction and hot deformation parameters. Generally speaking, lower hot compaction and deformation temperatures are preferable, since a high temperature will lead to decreased coercivity as a result of grain growth.

However, we observed that under some conditions, higher hot deformation temperatures resulted in higher ${}_MH_c$, higher B_r, and especially higher $(BH)_{max}$. Figure 1.36 shows magnetic properties of nanocomposite $Nd_2Fe_{14}B/\alpha$-Fe magnets versus the hot deformation temperature. Before hot compaction, the Nd-Fe-B powder particles were coated with Fe using electric coating for 1 hour. The hot compaction was performed at 560°C under around 25 kpsi. The hot deformation was performed at 960, 970, 980, and 1000°C under about 10 kpsi.

It can be seen from Figure 1.36 that when the hot deformation temperature is increased from 960 to 1000°C, ${}_MH_c$ is increased from 6.4 to 10.2 kOe, B_r from 9.9 to 10.3 kG, and $(BH)_{max}$ from 16.6 to 41.6 MGOe. The increase of $(BH)_{max}$ is as high as 150%. It seems that the relationship between magnetic properties and hot deformation temperature is not as simple as previously understood. The mechanism that is responsible for the interesting phenomenon observed during this project has yet to be further explored.

1.3 Advantage of the nanograin composite magnets

In addition to potentially much higher magnetic performance than conventional Nd-Fe-B magnets, the nanograin composite Nd-Fe-B/α-Fe or Nd-Fe-B/Fe-Co magnets also have potential lower cost. Figure 1.37 compares processes of (a) conventional sintered Nd-Fe-B magnets and (b) new nanograin composite Nd-Fe-B/α-Fe or Nd-Fe-B/Fe-Co magnets. It can be seen from Figure 1.37 that fewer steps are required to produce the new composite magnets. Further, in the conventional process of making sintered Nd-Fe-B magnets, since the particle size is around 3 micrometers after the milling, all steps must be performed in high vacuum or Ar atmosphere. In contrast, the particle size for the new composite magnets is around 300 micrometers. Therefore, after crushing, all process steps, including hot compaction and hot deformation, can be carried out in air without the need for any special protection, which will make the new process more cost effective.

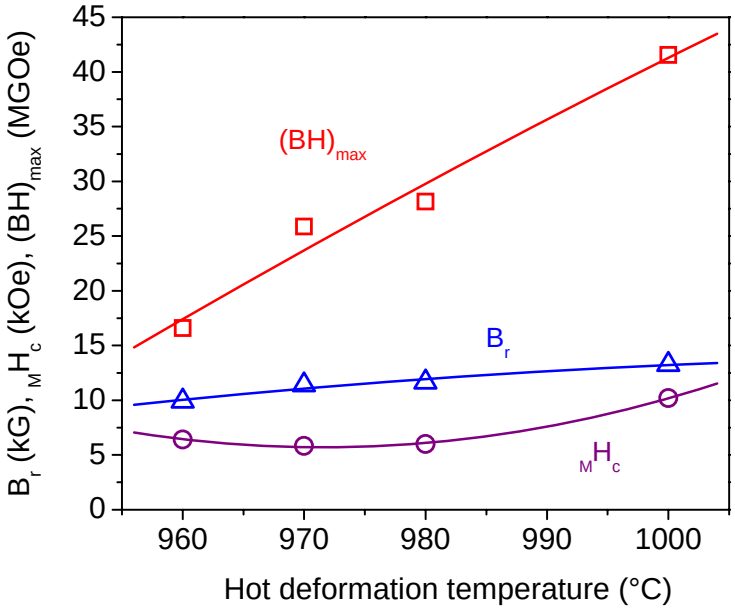

Fig. 1.36. Magnetic properties vs. hot deformation temperature.

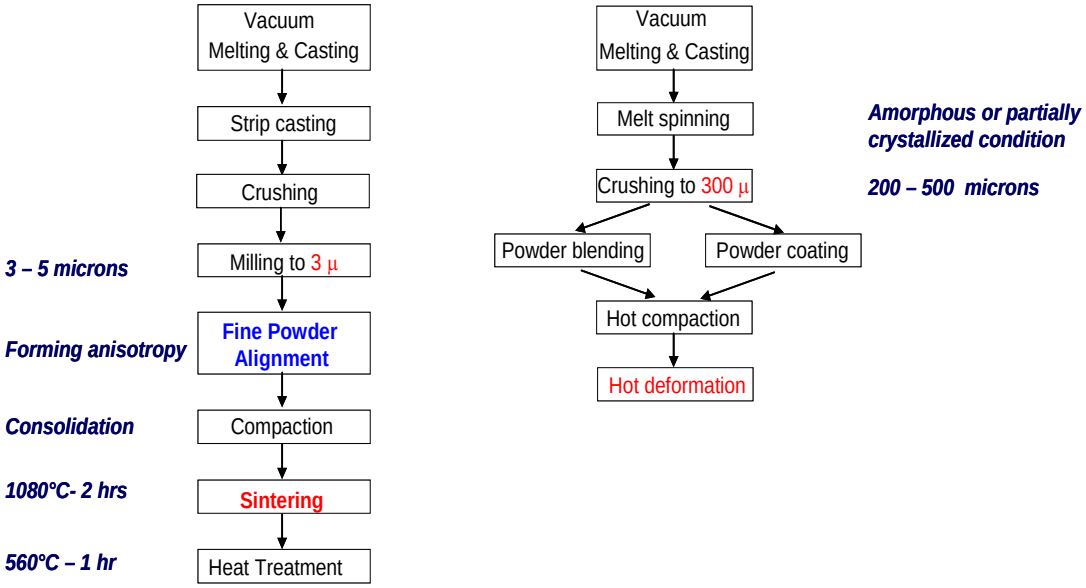

(a) (b)

Fig. 1.37. Comparison of processes of (a) conventional sintered Nd-Fe-B magnets; (b) new nanograin composite Nd-Fe-B/α-Fe or Nd-Fe-B/Fe-Co magnets.

The new composite magnets will have improved corrosion resistance. This is especially true for composite magnets prepared using various coating techniques, since the more corrosive Nd-Fe-B particles are enclosed in less corrosive α-Fe or Fe-Co layers. In addition, the new composite magnets will have improved fracture toughness because of the very fine nanograin structure and the existence of a relatively soft α-Fe or Fe-Co phase.

1.3.1 Problem with the current nanograin composite magnets

The x-ray diffraction analyses revealed variations in the degree of grain alignment of the upper and lower faces of the specimens, even in specimens with $(BH)_{max}$ in the 50 MGOe range. This phenomenon is believed to be related to the fact that only unidirectional stress was applied in the die upsetting process. The grain alignment on two surfaces of a few anisotropic nanocomposite magnets was analyzed using x-ray diffraction. The results indicated that in most cases there was a significant difference in the degree of grain alignment between the two surfaces. A typical example is shown in Figures 1.38 and 1.39. Figure 1.38 shows that one surface demonstrates very good grain alignment characterized by the enhanced intensity of (004), (006), and (008) peaks, and a greater than 1 intensity ratio of (006) over (105). On the other hand, another surface of the same specimen shows very poor grain alignment as shown in Figure 1.39.

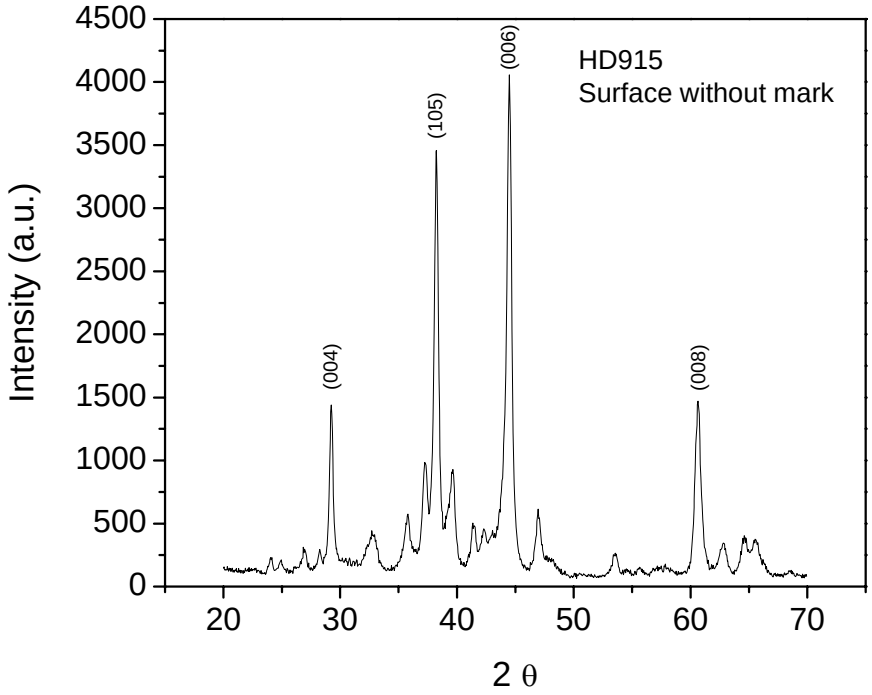

Fig. 1.38. XRD pattern of the no-mark surface of specimen HD915.

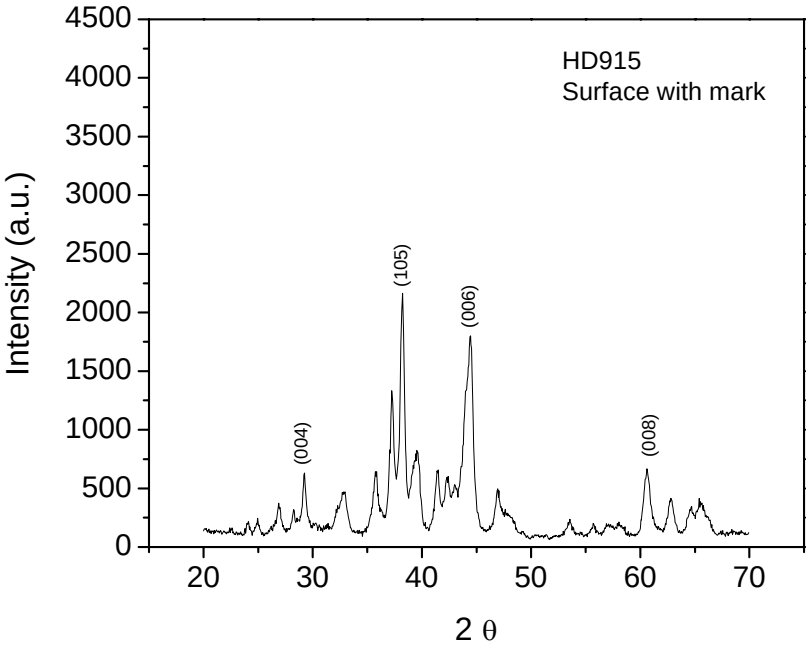

Fig. 1.39. XRD pattern of the mark surface of specimen HD915.

The magnetic properties of specimen HD915 (Figure 1.40), show that the $(BH)_{max}$ reaches 48 MGOe. This property is actually an average of a part with very good grain alignment and a part with poor grain alignment within the same magnet specimen.

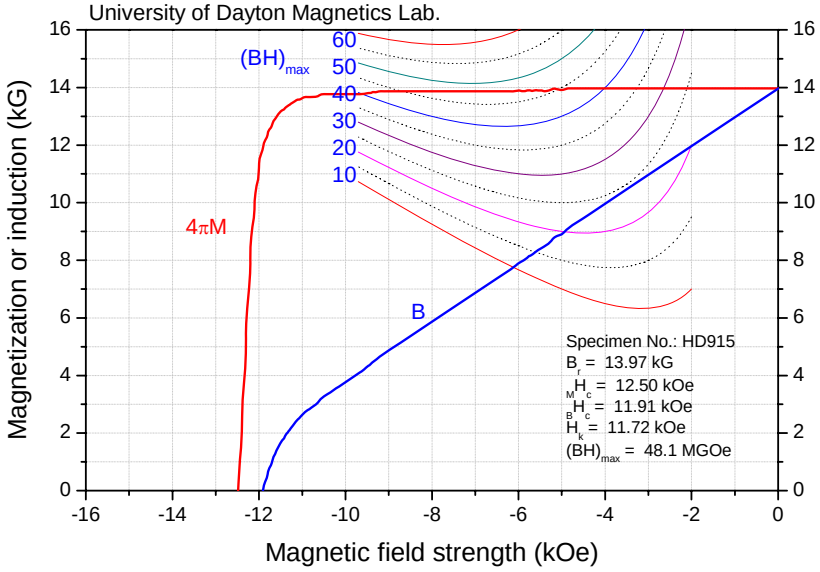

Fig. 1.40. Demagnetization curves of specimen HD915.

The non-uniform grain alignment is caused by non-uniform hot deformation. It is anticipated, therefore, that when more uniform grain alignment is reached much better magnetic properties can be accomplished.

2. Hybrid Nanograin $Pr_2(Fe,Co)_{14}B/Pr(Co,Fe)_5$ Magnets with Improved Thermal Stability

Nd-Fe-B magnets have excellent room temperature magnetic properties, but very poor thermal stability due to their low Curie temperature of 310°C. The magnetic properties of Nd-Fe-B magnets, especially intrinsic coercivity, sharply deteriorate with increasing temperature. On the other hand, sintered $Sm_2(Co,Fe,Cu,Zr)_{17}$ magnets demonstrate excellent thermal stability, but have a high price. Therefore, a wide gap in the operating temperature and thermal stability exists between the mainstream Nd-Fe-B magnets and $Sm_2(Co,Fe,Cu,Zr)_{17}$ magnets.

Hybrid nanograin $Nd_2Fe_{14}B/Sm_2(Co,Fe)_{17}$ magnets were successfully made at University of Dayton previously [6]. Research efforts have concentrated on hybrid nanograin $Pr_2Fe_{14}B/Pr(Co,Fe)_5$ magnets during the present project because of their very wide processing windows.

2.1 Nanograin $PrCo_5$ and $Pr(Co,Fe)_5$ magnets

In order to make a nanograin $PrCo_5$ magnet, a $PrCo_5$ alloy powder in an amorphous condition must first be obtained using mechanical alloying for 16 hours in an Ar atmosphere. The amorphous powder is then consolidated using rapid RF inductive hot compaction at around 600 to 750°C for 2 minutes under 25 kpsi in vacuum. It should be noted that the hot compaction process is not only a consolidation process, but also a crystallization process of the amorphous alloy. After the hot compaction, bulk fully dense isotropic nanocomposite magnets can be readily synthesized. Further hot deformation of the hot compacted isotropic nanocomposite results in anisotropic nanocomposite magnets.

Figure 2.1 shows demagnetization curves of a hot compacted isotropic $PrCo_5$ (blue curves) and demagnetization curves of the same magnet after hot deformation (red curves). A high intrinsic coercivity over 15 kOe was obtained after hot compaction. After hot deformation, the coercivity was reduced, while remanence increased and the maximum energy product, $(BH)_{max}$, was increased from 11.53 to 16.77 MGOe, indicating that at least partial grain alignment was formed during hot deformation. Repeated experiments led to similar results. With further development, $PrCo_5$ magnets with much higher intrinsic coercivity can be development since the anisotropy field of $PrCo_5$ is as high as 200 kOe, while improving hot deformation will lead to higher energy product.

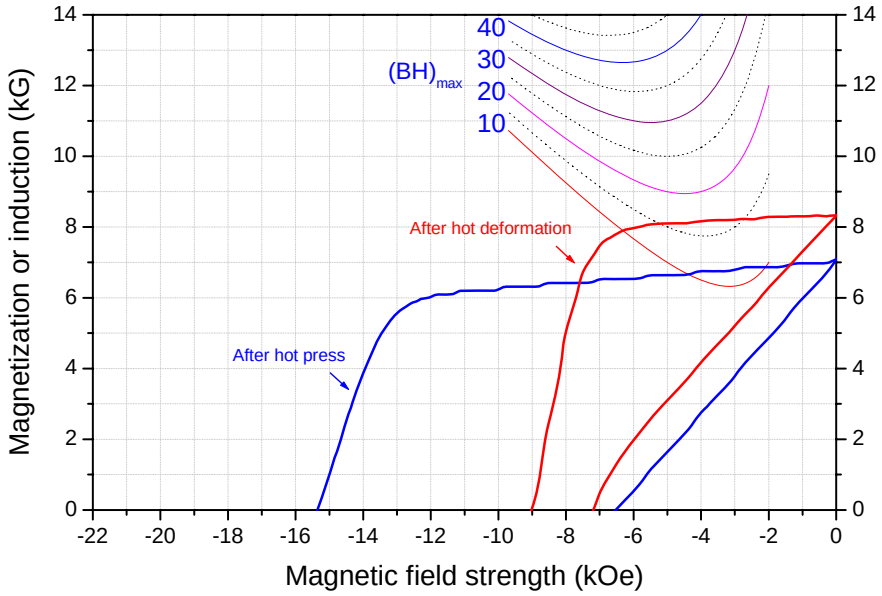

Figure 2.1. Demagnetization curves of hot compacted and hot deformed nanograin $PrCo_5$.

A partial substitution of Fe for Co in $PrCo_5$ was made to increase its magnetization and, hence, energy product. However, this substitution led to a sharp drop of ${}_MH_c$ and $(BH)_{max}$ of $PrCo_5$ as shown in Figure 2.2. But an increase of the maximum magnetization value, $(4\pi M)_{max}$, can be observed when 20% Fe is substituted for Co.

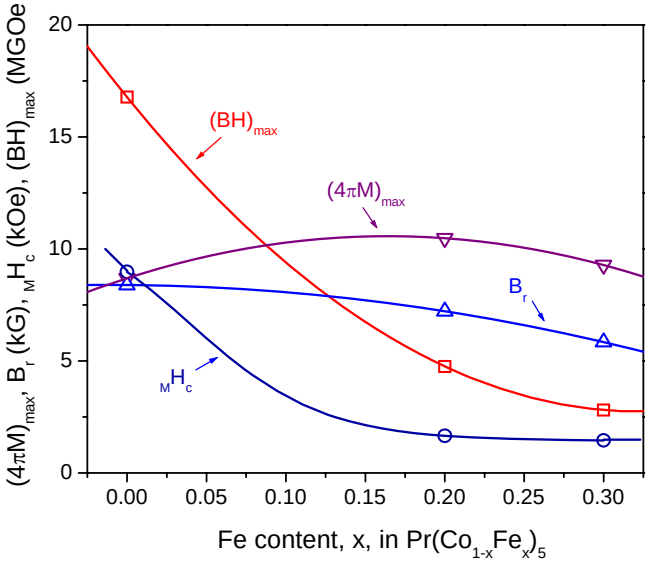

Figure 2.2. Effect of Fe content, x, in $Pr(Co_{1-x}Fe_x)_5$ on magnetic properties of $Pr(Co_{1-x}Fe_x)_5$.

2.2 Nanograin $Pr_2(Fe,Co)_{14}B$ magnets

$Pr_2(Fe,Co)_{14}B$ is an important component in a hybrid nanocomposite $Pr_2(Fe,Co)_{14}B$/ $PrCo_5$ magnet. Before a high-performance hybrid nanocomposite $Pr_2(Fe,Co)_{14}B/PrCo_5$ magnet can be made, the process conditions of a single nanograin $Pr_2(Fe,Co)_{14}B$ magnet have to be determined.

Figure 2.3 shows demagnetization curves of a nanograin $Pr_2(Fe_{0.94}Co_{0.06})_{14}B$ magnet after hot compaction and hot deformation. The magnet was compacted at 620°C for 2 minutes and hot deformed at 940°C for 2 minutes with 71% height reduction. The hot deformed magnet has a high remanence of 11.85 kG, a high maximum energy product of 33.32 MGOe, and very good squareness of the demagnetization curve.

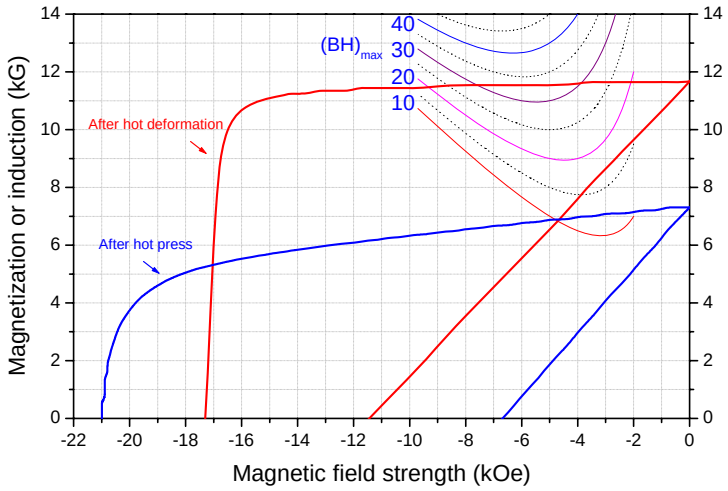

Figure 2.3. Demagnetization curves of hot compacted isotropic $Pr_2(Fe_{0.94}Co_{0.06})_{14}B$ and hot deformed anisotropic $Pr_2(Fe_{0.94}Co_{0.06})_{14}B$.

2.3 Nanocomposite $Pr_2(Fe,Co)_{14}B/PrCo_5$ and $Pr_2(Fe,Co)_{14}B/Pr(Co,Fe)_5$ magnets

2.3.1 Magnetic properties of nanocomposite $Pr_2(Fe,Co)_{14}B/PrCo_5$ and $Pr_2(Fe,Co)_{14}B/ Pr(Co,Fe)_5$ magnets

Since good magnetic properties were readily obtained in both nanograin $Pr_2(Fe_{0.94}Co_{0.06})_{14}B$ and $PrCo_5$ magnets, the same processing procedures were used to make hybrid nanocomposite $Pr_2(Fe_{0.94}Co_{0.06})_{14}B/PrCo_5$ magnets.

Demagnetization curves of a hybrid magnet containing 80 wt% $Pr_2(Fe_{0.94}Co_{0.06})_{14}B$ and 20% $PrCo_5$, denoted as $Pr_2(Fe_{0.94}Co_{0.06})_{14}B/PrCo_5$ [80 wt%/20 wt%], are shown in Figure 2.4. This specimen has a high ${}_MH_c$ over 16 kOe and $(BH)_{max}$ near 33 MGOe. Figure 2.5 demonstrates magnetic properties as a function of the fraction of the $PrCo_5$ component in the hybrid $Pr_2(Fe_{0.94}Co_{0.06})_{14}B/PrCo_5$ magnet. Figure 2.5 also indicates that when the fraction of $PrCo_5$ is increased to 40 wt% in the hybrid magnet, $(BH)_{max}$ dropped to around 24 MGOe, basically as a result of the drop of ${}_MH_c$.

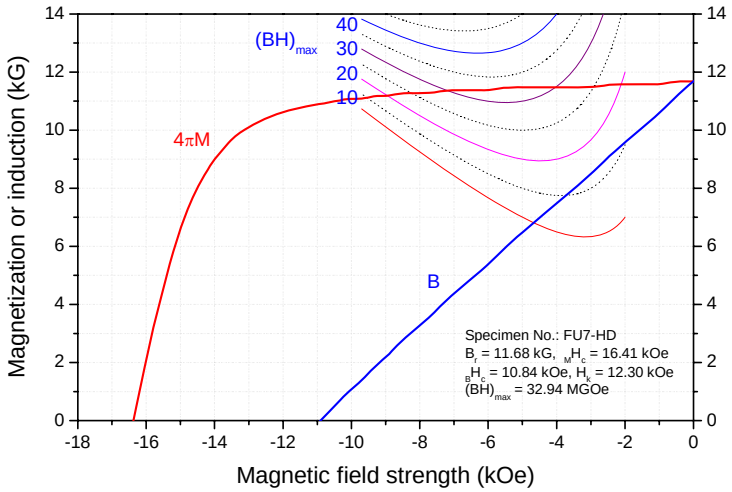

Figure 2.4. Demagnetization curves of the first bulk hot deformed nanocrystalline $Pr_2(Fe_{0.94}Co_{0.06})_{14}B/PrCo_5$ [80 wt%/20 wt%] magnet.

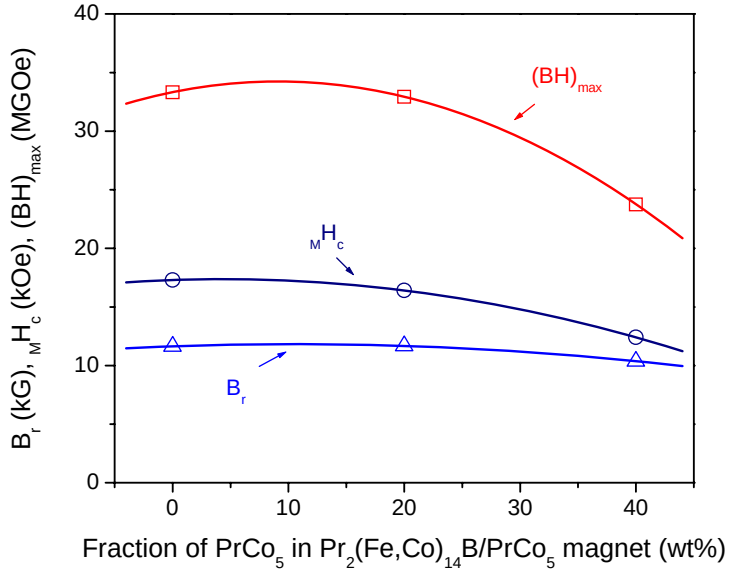

Figure 2.5. Magnetic properties as a function of the fraction of $PrCo_5$ in a hybrid $Pr_2(Fe_{0.94}Co_{0.06})_{14}B/PrCo_5$ magnet.

It was mentioned in previously that partial substitution of Fe for Co in $PrCo_5$ resulted in a sharp drop of both ${}_MH_c$ and $(BH)_{max}$. However, a surprising discovery was that partial substitution of Fe for Co in the $PrCo_5$ component of a hybrid nanocomposite $Pr_2(Fe_{0.94}Co_{0.06})_{14}B/Pr(Co,Fe)_5$ magnet leads to increased ${}_MH_c$, B_r, and $(BH)_{max}$. Figure 2.6 shows demagnetization curves of a hybrid nanocrystalline $Pr_2(Fe_{0.94}Co_{0.06})_{14}B/ Pr(Co_{0.8}Fe_{0.2})_5$ [80 wt%/20 wt%] magnet. The B_r of this hybrid magnet was increased to 12 kG and $(BH)_{max}$ was increased to 34.5 MGOe. At the same time, its intrinsic coercivity increased to near 17 kOe.

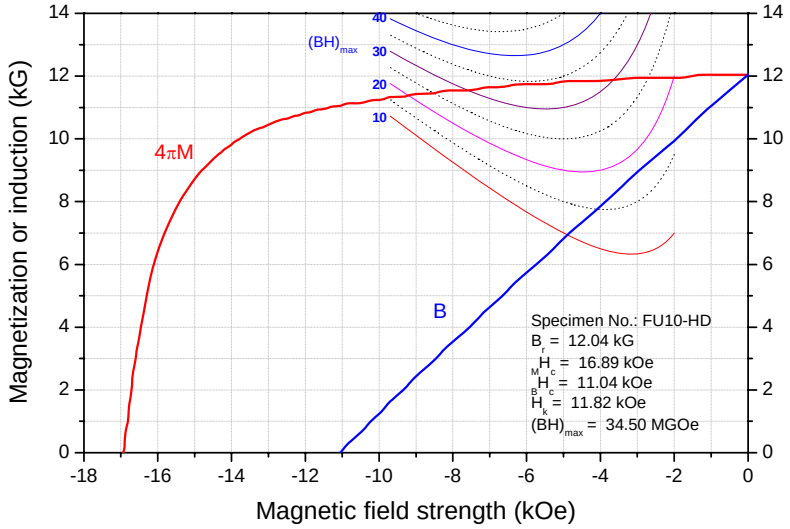

Figure 2.6. Demagnetization curves of the first bulk hot deformed nanocomposite $Pr_2(Fe_{0.94}Co_{0.06})_{14}B/Pr(Co_{0.8}Fe_{0.2})_5$ [80 wt%/20 wt%].

Figure 2.7 shows demagnetization curves of a bulk hot deformed nanocomposite $Pr_2(Fe_{0.94}Co_{0.06})_{14}B/ Pr(Co_{0.8}Fe_{0.3})_5$ [80 wt%/20 wt%]. The ${}_MH_c$ of this magnet is further increased to over 17 kOe while at the same time, high B_r and high $(BH)_{max}$ are maintained. Figure 2.8 summarizes the effect of Fe content, x, in $Pr_2(Fe,Co)_{14}B/ Pr(Co_{1-x}Fe_x)_5$ on $(4\pi M)_{max}$, B_r, ${}_MH_c$, and $(BH)_{max}$ of hybrid nanocrystalline $Pr_2(Fe,Co)_{14}B/Pr(Co_{1-x}Fe_x)_5$.

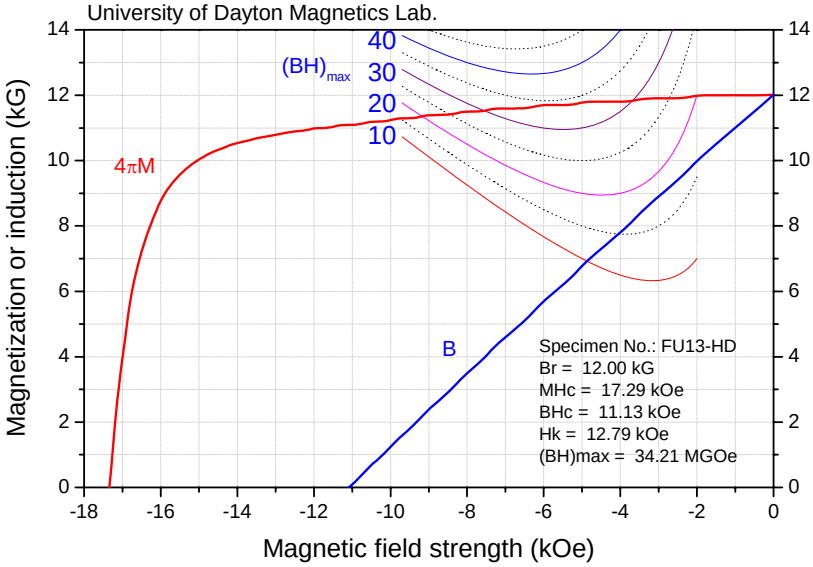

Figure 2.7. Demagnetization curves of the first bulk hot deformed nanocomposite $Pr_2(Fe_{0.94}Co_{0.06})_{14}B/Pr(Co_{0.8}Fe_{0.3})_5$ [80 wt%/20 wt%].

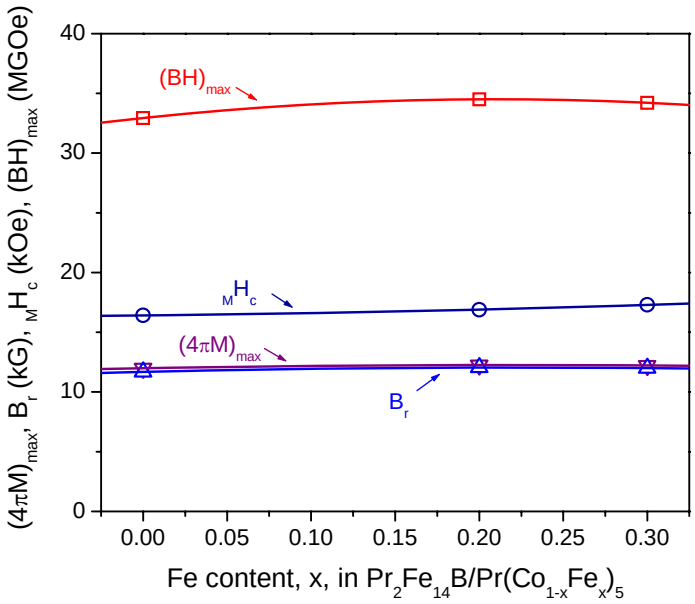

Figure 2.8. Effect of Fe content, x, in $Pr_2(Fe,Co)_{14}B/Pr(Co_{1-x}Fe_x)_5$ on $(4\pi M)_{max}$, B_r, $_MH_c$, and H_k of hybrid nanocrystalline $Pr_2(Fe,Co)_{14}B/Pr(Co_{1-x}Fe_x)_5$.

2.3.2 Thermal stability of nanocomposite $Pr_2(Fe,Co)_{14}B$/ $Pr(Co,Fe)_5$ magnets

Figure 2.9 shows the temperature coefficient of magnetic flux versus temperature for the following magnets: (a) $Pr_2(Fe_{0.94}Co_{0.06})_{14}B$; (b) $Pr(Co_{0.8}Fe_{0.2})_5$; (c) hybrid nanocrystalline $Pr_2(Fe_{0.94}Co_{0.06})_{14}B$/ $Pr(Co_{0.8}Fe_{0.2})_5$ [80 wt%/20 wt%]; and (d) $Pr_2(Fe_{0.94}Co_{0.06})_{14}B/Pr(Co_{0.8}Fe_{0.2})_5$ [60 wt%/40 wt%]. Assuming that a temperature coefficient of not worse than -0.10%/°C is required for a particular application, the highest operating temperature for $Pr_2(Fe_{0.94}Co_{0.06})_{14}B$ is only 40°C would satisfy this requirement. The operating temperatures can be increased to 90 and 175°C, respectively, if the hybrid $Pr_2(Fe_{0.94}Co_{0.06})_{14}B$/ $Pr(Co_{0.8}Fe_{0.2})_5$ [80 wt%/20 wt%] and $Pr_2(Fe_{0.94}Co_{0.06})_{14}B$/ $Pr(Co_{0.8}Fe_{0.2})_5$ [60 wt%/40 wt%] are used.

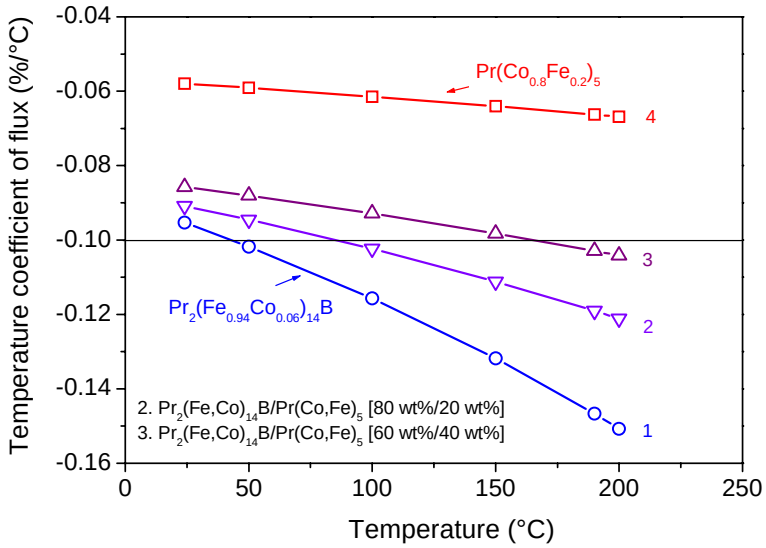

Figure 2.9. Temperature coefficient of magnetic flux versus temperature for (a) $Pr_2(Fe_{0.94}Co_{0.06})_{14}B$; (b) hybrid $Pr_2(Fe_{0.94}Co_{0.06})_{14}B/Pr(Co_{0.8}Fe_{0.2})_5$ [80 wt%/20 wt%]; (c) hybrid $Pr_2(Fe_{0.94}Co_{0.06})_{14}B/Pr(Co_{0.8}Fe_{0.2})_5$ [60 wt%/40 wt%]; and (d) $Pr(Co_{0.8}Fe_{0.2})_5$.

2.3.3 Microstructure of nanocomposite $Pr_2(Fe,Co)_{14}B$/ $Pr(Co,Fe)_5$ magnets

Figure 2.10 shows SEM micrographs of an anisotropic hybrid $Pr_2(Fe_{0.94}Co_{0.06})_{14}B$/ $Pr(Co_{0.8}Fe_{0.2})_5$ [60 wt%/40 wt%] magnet. It can be seen from Figure 2.10(a) that the grain size in this magnet is not uniform. In addition to small grains, there are some large grains in the micrometer range. Figure 2.10(b) is a high resolution SEM image showing elongated and aligned grains. It can be seen that the long axes of some grains are over 500 nm. With further reductions in the grain size, better magnetic performance is anticipated.

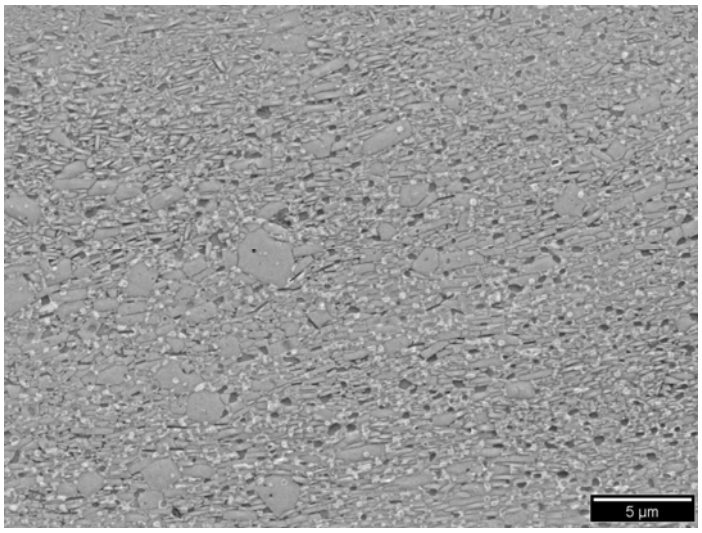

(a)

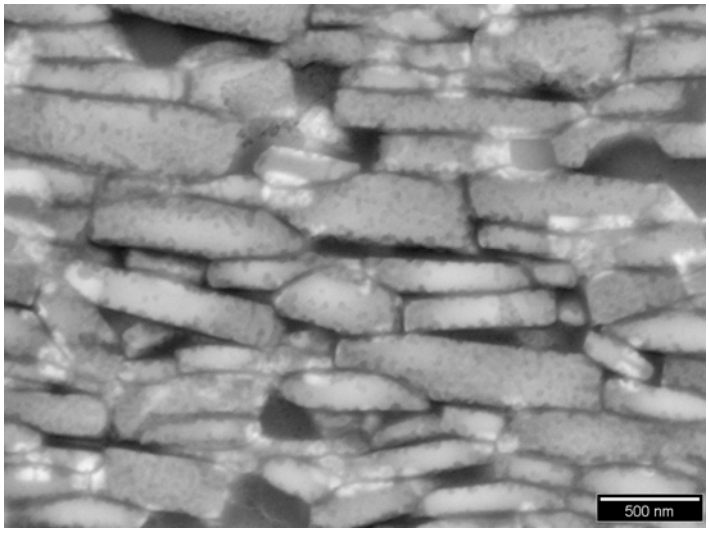

(b)

Figure 2.10. SEM micrographs of anisotropic hybrid $Pr_2(Fe_{0.94}Co_{0.06})_{14}B/Pr(Co_{0.8}Fe_{0.2})_5$ [60 wt%/40 wt%]with small (a) and large magnifications (b).

2.3.4 Novel coercivity enhancement after hot deformation

An abnormal increase of $_{M}H_{c}$ after hot deformation in the hybrid nanocrystalline $Pr_2(Fe,Co)_{14}B/Pr(Co,Fe)_5$ system was observed. In a normal case, after a hot pressed isotropic magnet is further hot deformed to an anisotropic magnet, its $_{M}H_{c}$ will be decreased by 20 to 40% as a result of grain growth, as shown in Figures 2.1 and 2.3.

However, an increase of $_{M}H_{c}$ in the hybrid nanocrystalline $Pr_2(Fe,Co)_{14}B/Pr(Co,Fe)_5$ system was observed after hot deformation as shown in Figures 2.11 through 2.13. It can be seen from Figure 2.12 that after hot deformation the intrinsic coercivity of $Pr_2(Fe_{0.94}Co_{0.06})_{14}B/Pr(Co_{0.5}Fe_{0.5})_5$ [80 wt%/20 wt%] increased from 15.14 to 15.53 kOe. As for $Pr_2(Fe_{0.94}Co_{0.06})_{14}B/Pr(Co_{0.8}Fe_{0.2})_5$ [60 wt%/40 wt%], its intrinsic coercivity increased from 11.23 to 15.84 as shown in Figure 2.13. It can be seen from Figure 2.13 that the hot pressed isotropic $Pr_2(Fe_{0.94}Co_{0.06})_{14}B/Pr(Co_{0.7}Fe_{0.3})_5$ [60 wt%/40 wt%] magnet has a low $_{M}H_{c}$ value of 8.5 kOe. After hot deformation, its $_{M}H_{c}$ increased to 17 kOe! This abnormal enhancement of $_{M}H_{c}$ may have the same origin as the $_{M}H_{c}$ increase shown in Figure 2.8. It is certainly related to the interaction between the $Pr_2(Fe,Co)_{14}B$ and $Pr(Co,Fe)_5$ phases.

Both XRD and SEM/EDS were performed in an attempt to explain the abnormal coercivity enhancement of the nanocomposite $Pr_2(Fe,Co)_{14}B/Pr(Co,Fe)_5$ magnets after hot deformation. One possible reason may be related to the fact that since the inductive hot press process was performed at a relatively low temperature of around 600°C for only 2 minutes, the amorphous $Pr_2(Fe,Co)_{14}B/Pr(Co,Fe)_5$ powder may be only partially crystallized, leading to low coercivity. After the subsequent hot deformation, the magnet alloy is fully crystallized and thus demonstrates increased coercivity.

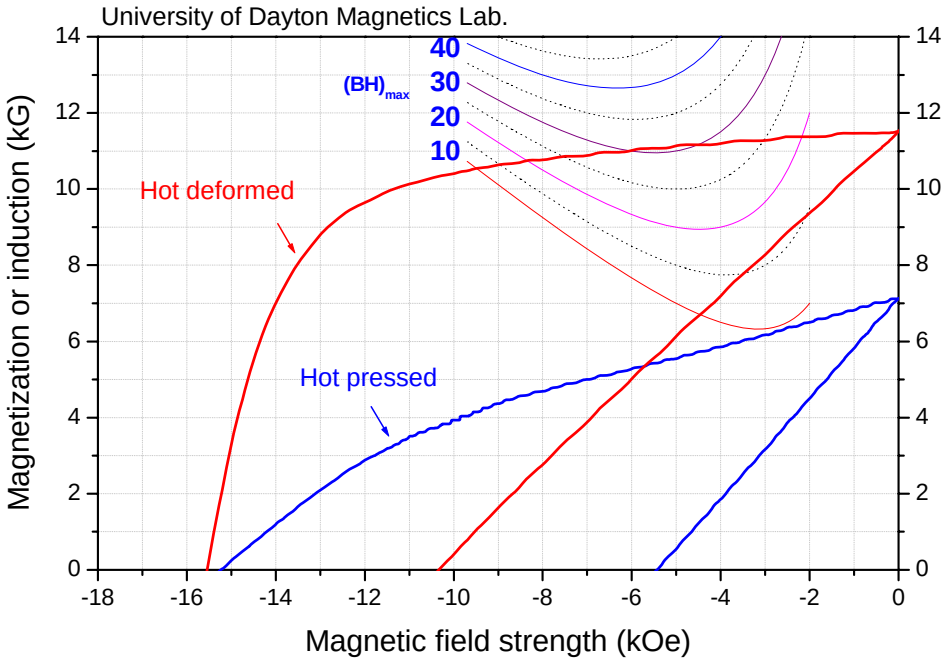

Figure 2.11. Demagnetization curves of hot pressed and hot deformed $Pr_2(Fe_{0.94}Co_{0.06})_{14}B/Pr(Co_{0.5}Fe_{0.5})_5$ [80 wt%/20 wt%].

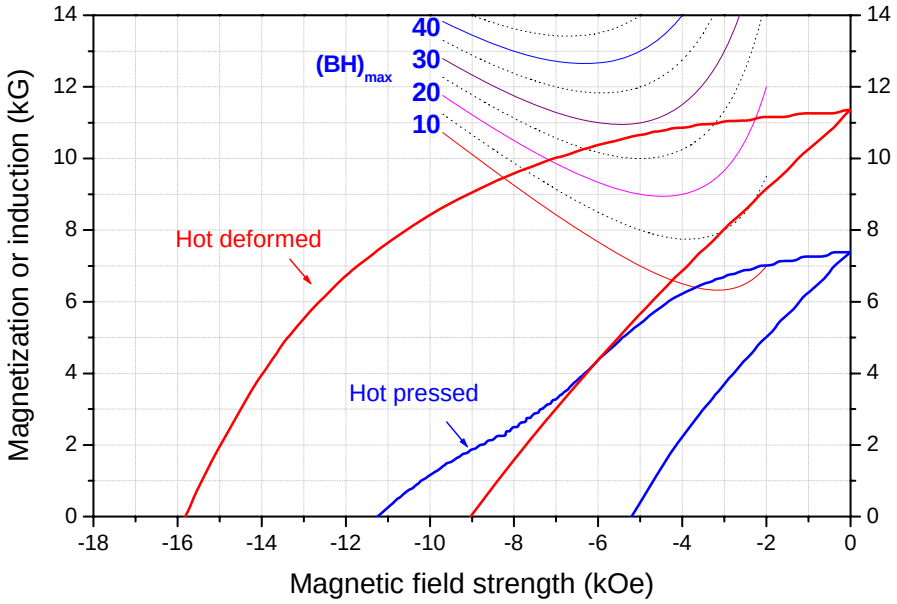

Figure 2.12. Demagnetization curves of hot pressed and hot deformed $Pr_2(Fe_{0.94}Co_{0.06})_{14}B/Pr(Co_{0.8}Fe_{0.2})_5$ [60 wt%/40 wt%].

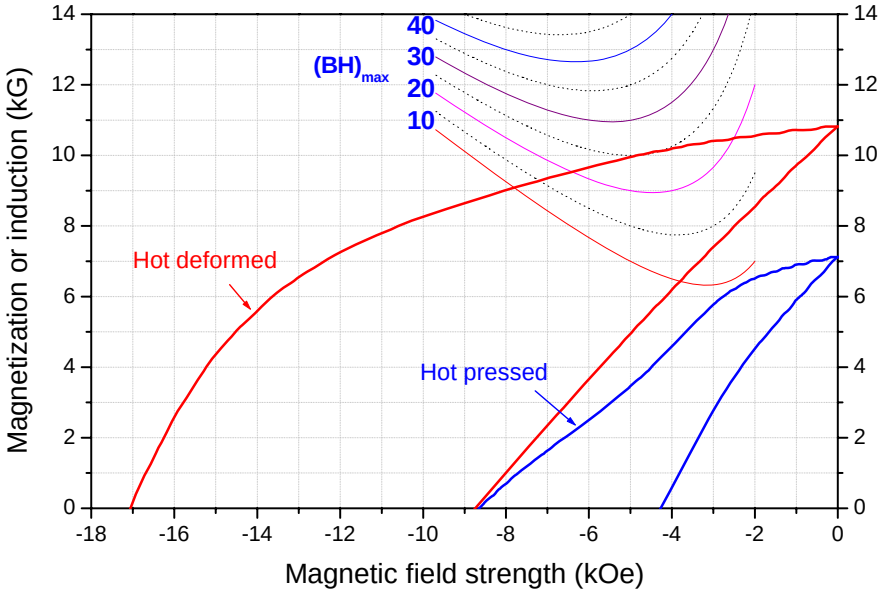

Figure 2.13. Demagnetization curves of hot pressed and hot deformed $Pr_2(Fe_{0.94}Co_{0.06})_{14}B/Pr(Co_{0.7}Fe_{0.3})_5$ [60 wt%/40 wt%].

However, XRD analyses did not strongly support this assumption. Figure 2.14 shows the XRD pattern of the as-mechanically alloyed powder of $Pr_2(Fe_{0.94}Co_{0.06})_{14}B/Pr(Co_{0.7}Fe_{0.3})_5$ [60 wt%/40 wt%]. It is in an amorphous condition except for an α-Fe peak. The XRD pattern of the same alloy powder after the hot press is given in Figure 2.15. Basically, the amorphous powder is fully crystallized after the hot press, though it has very fine grain structure as indicated by the wide half-peak width as shown in Figure 2.15.

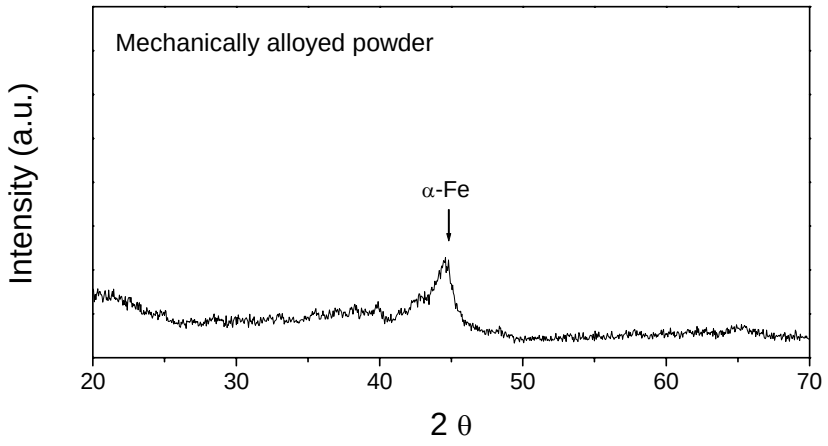

Figure 2.14. XRD pattern of a powder mixture of $Pr_2(Fe_{0.94}Co_{0.06})_{14}B/Pr(Co_{0.7}Fe_{0.3})_5$ [60 wt%/40 wt%] after mechanical alloying.

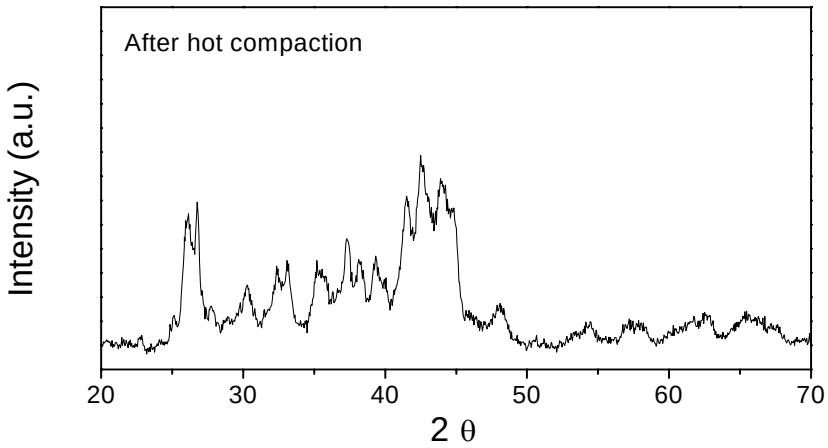

Figure 2.15. XRD pattern of hot compacted $Pr_2(Fe_{0.94}Co_{0.06})_{14}B/Pr(Co_{0.7}Fe_{0.3})_5$ [60 wt%/40 wt%].

Grain growth and texture formation take place in the hot deformation process. Figures 2.16 and 2.17 show XRD patterns of two surfaces of the hot deformed anisotropic magnet specimen. Apparently, two surfaces of the same specimen demonstrate a different degree of grain alignment. These results indicate that the abnormal coercivity enhancement cannot be explained by crystallization of an amorphous material during hot deformation.

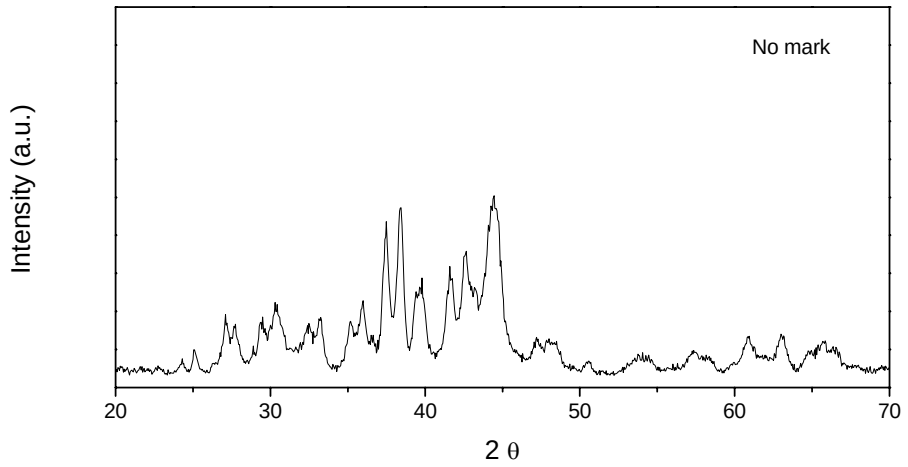

Figure 2.16. XRD pattern of a hot deformed $Pr_2(Fe_{0.94}Co_{0.06})_{14}B/Pr(Co_{0.7}Fe_{0.3})_5$ [60 wt%/40 wt%] on the no mark surface, showing crystallized 2:14:1 and 1:5 phases with relatively poor grain alignment.

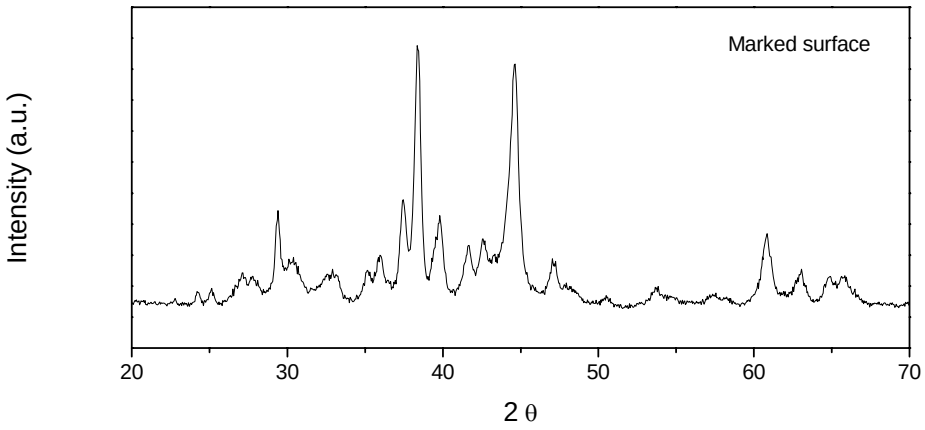

Figure 2.17. XRD pattern of the hot deformed $Pr_2(Fe_{0.94}Co_{0.06})_{14}B/Pr(Co_{0.7}Fe_{0.3})_5$ [60 wt%/40 wt%] on the marked surface, showing crystallized 2:14:1 and 1:5 phases with good grain alignment.

Figure 2.18 shows the temperature dependence of magnetic moment of hot deformed $Pr_2(Fe_{0.94}Co_{0.06})_{14}B/Pr(Co_{0.7}Fe_{0.3})_5$ [60 wt%/40wt%]. Two major events were detected: one at 505°C and the other at 975°C. Most likely, 505°C is the Curie temperature of a main phase, while 975°C is the Curie temperature of a minor phase. In addition, a few minor events were detected at 313, 772, and 872°C, respectively.

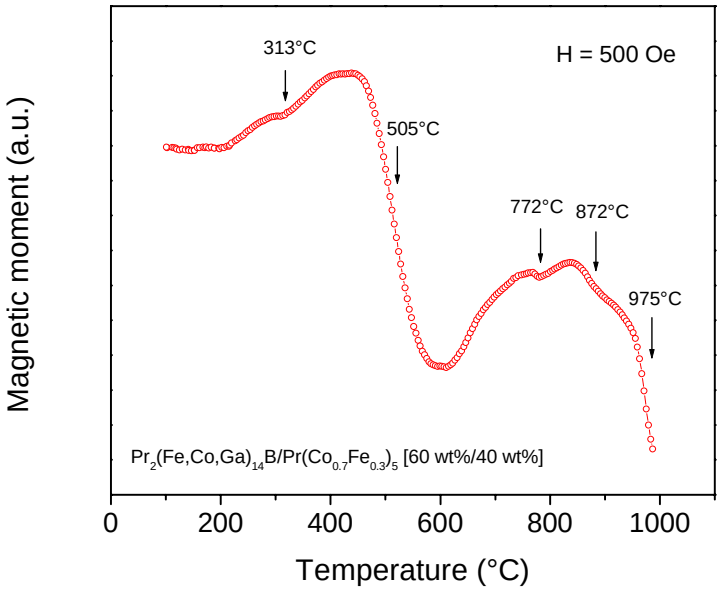

Figure 2.18. Temperature dependence of magnetic moment of $Pr_2(Fe_{0.94}Co_{0.06})_{14}B/Pr(Co_{0.7}Fe_{0.3})_5$ [60 wt%/40wt%], showing two major events at 505°C and 975°C and minor events.

SEM/EDS analyses were performed to identify the existing phases in the nanocomposite magnets. Figure 2.19 shows a SEM backscattered electron image of the magnet. Figure 2.20 shows three zones identified in the microstructure. The composition of each zone was determined using SEM/EDS and the results are given in Table 2-1. According to SEM/EDS, the three zones correspond to $Pr(Co_{0.7}Fe_{0.3})_5$, $Pr_2(Co_{0.6}Fe_{0.4})_7$, and $Pr_2(Fe_{0.7}Co_{0.3})_{14}B$, respectively.

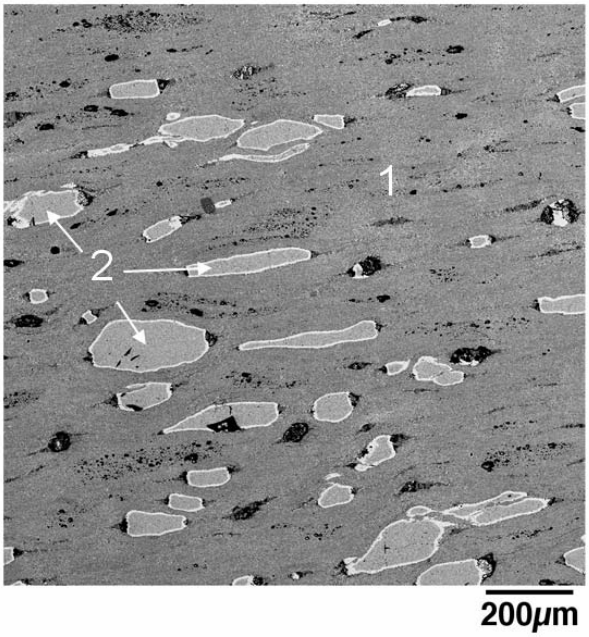

Figure 2.19. SEM backscattered electron image of $Pr_2(Fe_{0.94}Co_{0.06})_{14}B/Pr(Co_{0.7}Fe_{0.3})_5$ [60 wt%/40wt%] after hot deformation, showing 2:14:1 matrix phase and 1:5 minor phase.

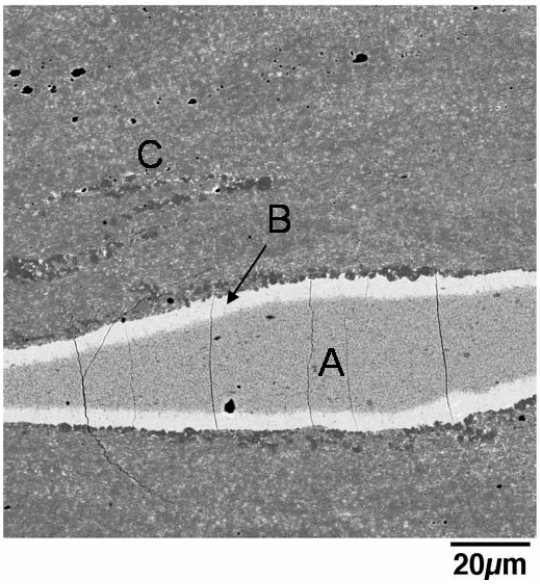

Figure 2.20. Three zones in the microstructure of $Pr_2(Fe_{0.94}Co_{0.06})_{14}B/Pr(Co_{0.7}Fe_{0.3})_5$ [60 wt%/40wt%].

Table 2-1. Compositions of Three Zones Obtained from SEM/EDS Analyses

Zone	Pr (at%)	Fe (at%)	Co (at%)	3d/R	Co/Fe	Possible phase
A	14.4	26.8	58.7	5.9	2.33	$Pr(Co_{0.7}Fe_{0.3})_5$
B	20.4	28.5	50.1	3.8	1.50	$Pr_2(Co_{0.6}Fe_{0.4})_7$
C	12.2	64.5	23.3	7.2	0.43	$Pr_2(Fe_{0.7}Co_{0.3})_{14}B$

It is interesting to note that a Pr-rich $Pr_2(Co_{0.6}Fe_{0.4})_7$ phase was formed after hot deformation. It has been reported that the Sm_2Co_7 compound has much lower anisotropy field than $SmCo_5$ and Sm_2Co_{17} compounds. No data have been seen for the anisotropy field value of the Pr_2Co_7 compound. However, if the trend of the anisotropy field variation in the Pr-Co system is similar to that in the Sm-Co system, then Pr_2Co_7 should have a low anisotropy field and, thus, cannot be responsible for the significantly enhanced coercivity after hot deformation.

These preliminary SEM/EDS results cannot fully account for the thermal magnetic analysis as shown in Figure 2.18 and the mechanism of the enhanced coercivity after hot deformation in nanocomposite $Pr_2(Fe,Co)_{14}B/Pr(Co,Fe)_5$, as indicated in Figures 2.11 through 2.13, remains unknown.

2.3.5. Long-term stability of the nanograin structure of hybrid nanocomposite magnets

Since the hybrid nanocomposite magnets are supposed to be used either in the case of temperature variation or at elevated temperatures from 80 to 250°C, the long-term stability of the nanograin structure would be a great concern.

Limited by the short time of the project, a long-term aging experiment was not performed for hybrid nanocomposite $Pr_2(Fe,Co)_{14}B/ Pr_2(Co,Fe)_{17}$ magnets. However, a similar experiment was carried out for a few nanocomposite $Nd_2(Fe,Co)_{14}B/Sm_2(Co,Fe)_{17}$ magnets. Figure 2.21 shows variation of the magnetic flux for a nanocomposite $Nd_2(Fe_{0.94}Co_{0.06})_{14}B/Sm_2(Co_{0.7}Fe_{0.3})_{17}$ [80 wt%/20 wt%] magnet with L/D = 1

aged at 100°C in air for over 5000 hours. This experiment clearly demonstrates that the magnetic flux is very stable during this long-term aging experiment, indicating little microstructure change. It is then anticipated that the hybrid nanocomposite $Pr_2(Fe,Co)_{14}B$/ $Pr_2(Co,Fe)_{17}$ magnets should have similar long-term structure stability.

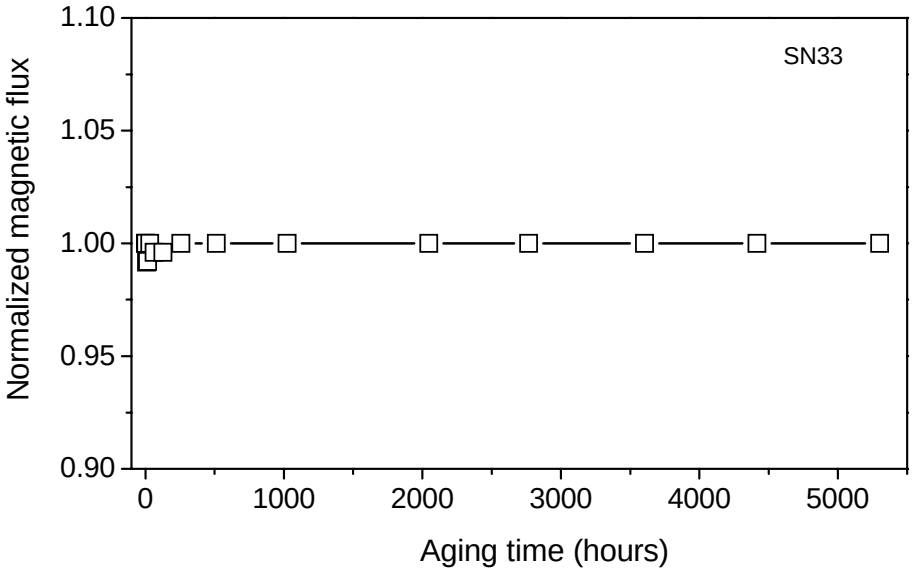

Figure 2.21. Result of a long-term aging experiment of a nanocomposite $Nd_2(Fe_{0.94}Co_{0.06})_{14}B/Sm_2(Co_{0.7}Fe_{0.3})_{17}$ [80 wt%-20 wt%] magnet with L/D = 1 aged at 100°C in air.

3. Nanograin Composite $Sm_2(Co,Fe)_{17}$/Fe-Co Magnets

Efforts have been made to apply the same technologies developed in nanograin composite $Nd_2Fe_{14}B/\alpha$-Fe or $Nd_2Fe_{14}B$/Fe-Co magnets to making nanograin composite $Sm_2(Co,Fe)_{17}$/Fe-Co magnets. Figure 3.1 shows a comparison of the processes used to make nanograin composite $Sm_2(Co,Fe)_{17}$/Fe-Co and conventional sintered $Sm_2(Co,Fe,Cu,Zr)_{17}$ magnets. The advantage of making new nanograin composite $Sm_2(Co,Fe)_{17}$/Fe-Co magnets is obvious. However, we have observed that the desired crystallographic texture is not as easy to obtain in $Sm_2(Co,Fe)_{17}$/Fe-Co. As a result, the highest $(BH)_{max}$ obtained in nanograin composite $Sm_2(Co,Fe)_{17}$/Fe-Co magnets is only around 14 MGOe. These results were summarized in the final report for Task No. 05-S530-0030-01-C1.

We have also attempted to combine the technologies used to make nanograin $Sm_2(Co,Fe)_{17}$ and conventional $Sm_2(Co,Fe,Cu,Zr)_{17}$ magnets, to take advantage of the high coercivity of the $Sm_2(Co,Fe,Cu,Zr)_{17}$ magnets. A bulk $Sm(Co_{0.75}Fe_{0.11}Cu_{0.11}Zr_{0.03})_{7.3}$ specimen was prepared using mechanical alloying with the starting materials under argon for 16 hours, followed by hot pressing at 650°C for 2 minutes with height reduction of 71%. Demagnetization curves of the hot pressed $Sm(Co_{0.75}Fe_{0.11}Cu_{0.11}Zr_{0.03})_{7.3}$ are given in Figure 3.2.

After hot pressing, the specimen was further hot deformed at 980°C for 14 minutes. The hot deformed demagnetization curves of $Sm(Co_{0.75}Fe_{0.11}Cu_{0.11}Zr_{0.03})_{7.3}$ are shown in Figure 3.3.
It can be seen from comparing Figures 3.2 and 3.3 that after the hot deformation B_r increases from 5.27 to 5.79 kG (~10% increase), $(BH)_{max}$ increases from 6.54 to 8.26 MGOe (26% increase), while $_MH_c$ decreases from 13.41 to 7.58 kOe.

After the hot deformation, a solid solution heat treatment was performed at 1190°C for 5 hours followed by a fast quenching to room temperature. Then, the specimen was aged at 820°C for 24 hours followed by a slow cooling at 1°C/minute to 400°C. Figure 3.4 demonstrates demagnetization curves of this specimen after the heat treatment. It can be seen from Figure 3.4 that $_{M}H_{c}$ increases from 7.58 to 21.3 kOe, as expected. Surprisingly, B_r increases from 5.79 to 7.12 kG (23% increase), and $(BH)_{max}$ increases from 8.26 to 11.42 MGOe (38% increase). The coercivity increase can be explained by the formation of a fine-scale cellular structure as in conventional 2:17 type magnets; however, the increase of B_r and $(BH)_{max}$ is unknown. It may relate to the selective grain growth, which is that grains with good alignment grow at the expense of misaligned grains.

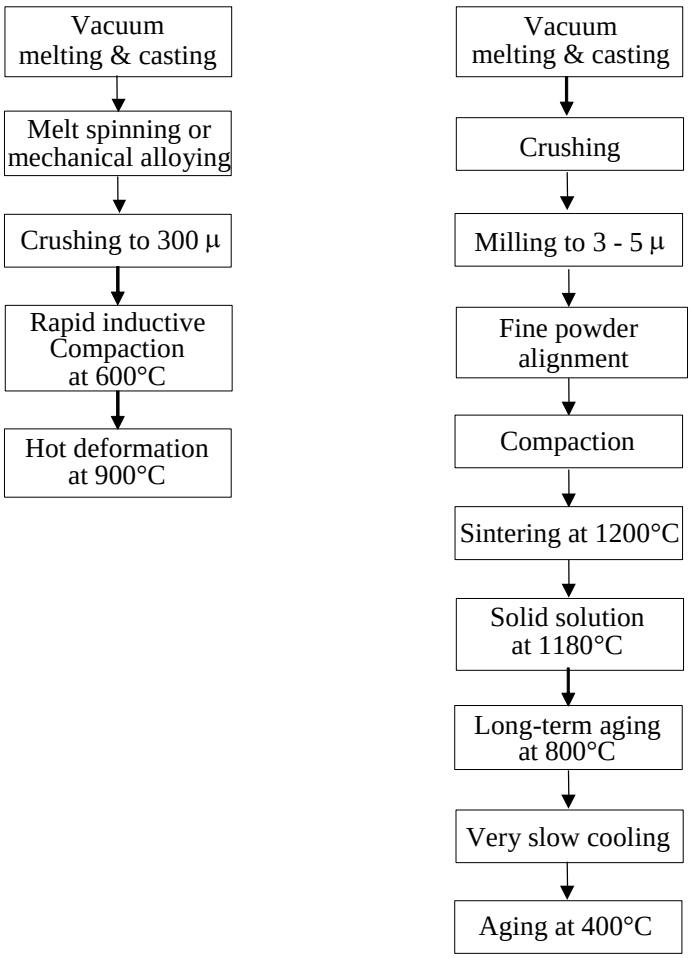

Figure 3.1. Comparison of processes used to make nanograin composite $Sm_2(Co,Fe)_{17}$/Fe-Co (a) and conventional sintered $Sm_2(Co,Fe,Cu,Zr)_{17}$ magnets (b).

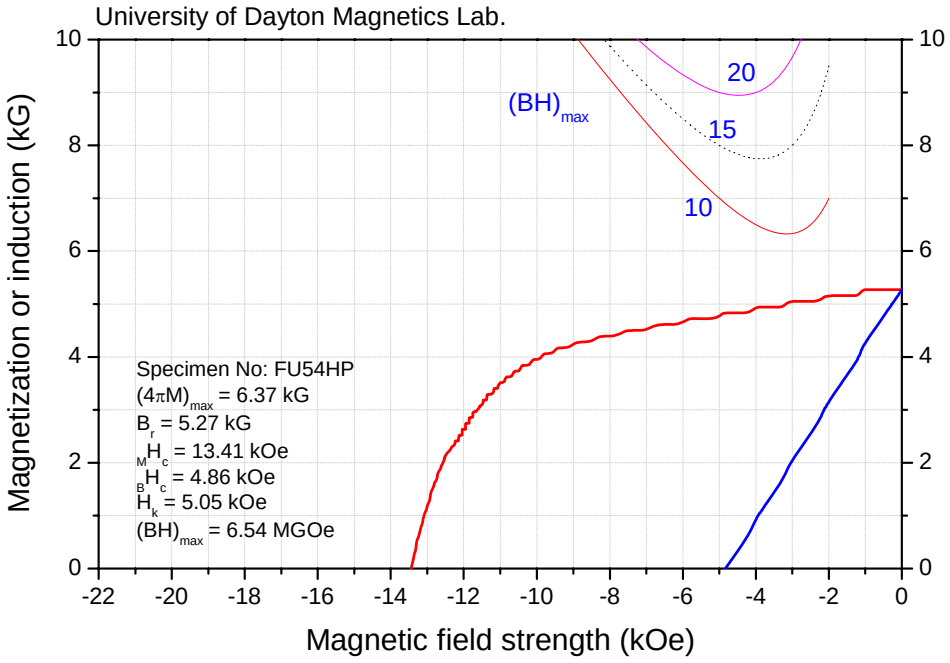

Fig. 3.2. Demagnetization curves of hot pressed $Sm(Co_{0.75}Fe_{0.11}Cu_{0.11}Zr_{0.03})_{7.3}$.

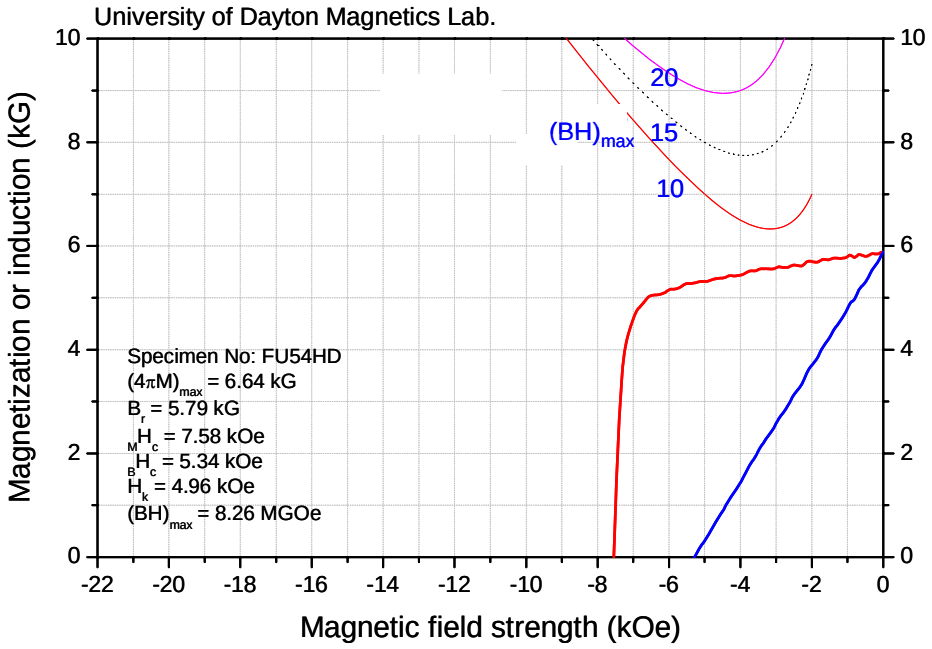

Fig. 3.3. Demagnetization curves of hot deformed $Sm(Co_{0.75}Fe_{0.11}Cu_{0.11}Zr_{0.03})_{7.3}$.

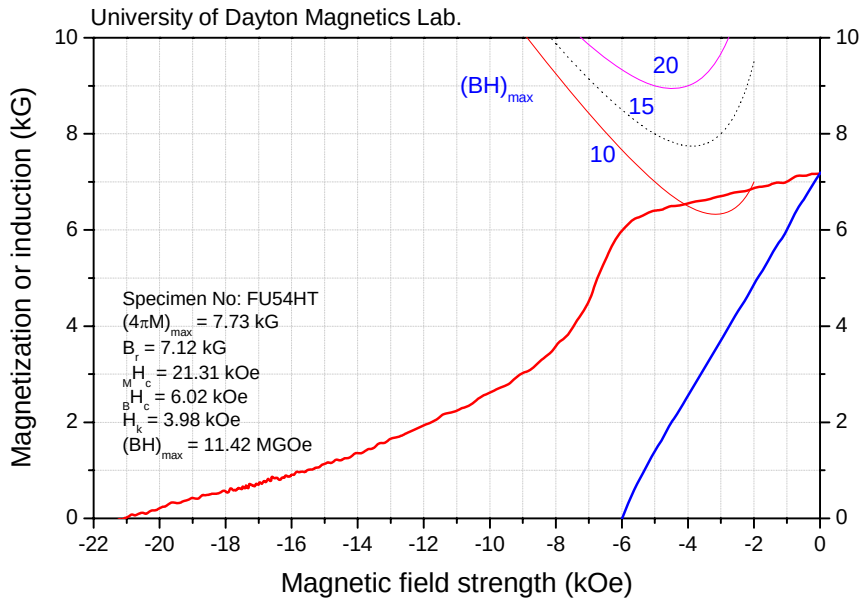

Fig. 3.4. Demagnetization curves of hot deformed $Sm(Co_{0.75}Fe_{0.11}Cu_{0.11}Zr_{0.03})_{7.3}$ after subsequent heat treatment.

4. Conclusions

(1) High-performance bulk anisotropic nanograin composite $Nd_2Fe_{14}B/\alpha$-Fe and $Nd_2Fe_{14}B$/Fe-Co magnets were successfully synthesized using hot compacting blended Nd-Fe-B and α-Fe or Fe-Co powders followed by subsequent hot deformation The Nd-Fe-B powders used comprise a minor Nd-rich phase and were prepared by melt spinning. The α-Fe or Fe-Co powders used were commercial products with micrometer size up to 50 micrometers. $(BH)_{max}$ of composite magnets prepared suing this technique could each 45 – 55 MGOe. The magnetically soft phase in these composite magnets is very large up to 40 micrometers.

(2) The upper dimension limit of the magnetically soft phase in a nanograin composite magnet can be as large as up to 40 micrometers. This is more than 1000 times larger than that predicted by previous models of interface exchange coupling in nanocomposite magnets, indicating that the interface exchange coupling at a hard/soft interface is actually much stronger than what people previously understood.

(3) High-performance bulk anisotropic nanograin composite $Nd_2Fe_{14}B/\alpha$-Fe and $Nd_2Fe_{14}B$/Fe-Co magnets were also successfully synthesized using hot compacting α-Fe or Fe-Co coated Nd-Fe-B powders followed by subsequent hot deformation. The Nd-Fe-B powders used comprise a minor Nd-rich phase and were prepared by melt spinning. The powder coating techniques used include DC and RF sputtering, pulsed laser deposition, chemical coating, and electrolyte coating. $(BH)_{max}$ of composite magnets prepared suing these techniques could each 45 – 55 MGOe.

(4) Bulk anisotropic hybrid nanograin $Pr_2Fe_{14}B/PrCo_5$ magnets with $(BH)_{max}$ = 34.5 MGOe and with improved thermal stability were synthesized. These magnets combine high magnetic performance of the $Pr_2Fe_{14}B$ and excellent thermal stability of $PrCo_5$ and can be used in applications in which the operating temperature and temperature coefficients of magnetic properties beyond Nd-Fe-B magnets are required

(5) It is difficult to create a desired crystallographic texture in nanograin composite $Sm_2(Co,Fe)_{17}$/Fe-Co magnets by hot deformation. However, combining technologies developed in nanograin magnets and conventional $Sm_2(Co,Fe,Cu,Zr)_{17}$ may open up a new avenue for future high-temperature $Sm_2(Co,Fe)_{17}$-based magnets.

5. References

[1] J.J. Croat, "Current Status of Rapidly Solidified Nd-Fe-B Permanent Magnets," *Proc. 11th Int'l. Workshop on REM*, ed. S.G. Sankar, Vol. 1, 1 (1990).

[2] D. Lee, J.S. Hilton, C.H. Chen, M.Q. Huang, Y. Zhang, G.C. Hadjipanayis, and S. Liu, "Bulk Isotropic and Anisotropic Rare Earth Magnets," *IEEE Trans. on Magn*. 40 (5), 2904 (2004).

[3] E.F. Kneller and R. Hawig, "The Exchange-Spring Magnet: A New Material Principle for Permanent Magnets," *IEEE Trans. Magn.* 27, 3588 (1991).

[4] R. Skomski and J.M.D. Coey, "Giant Energy Product in Nanostructured Two-phase Magnets," *Phys. Rev*. B 48, 15812 (1993).

[5] A. Manaf, R.A. Buckley, and H.A. Davies, "New Nanocrystalline High-remanence Nd-Fe-B Alloys by Rapid Solidification," *J. Magn. Magn. Mater*. 128, 302 (1993).

[6] D. Lee, C.H. Chen, S. Liu, and M.Q. Huang, "Nanocomposite Rare Earth Magnets," *Proc. 18th Workshop on HPM*, Vol. 2, 667 (2004).